Influence of catalyst supports on H2-SCR catalysts: A combined experimental and modeling approach including mass transfer

Applied Catalysis B: Environment and Energy 395 (2026) 126855

Contents lists available at ScienceDirect

Applied Catalysis B: Environment and Energy

journal homepage: www.elsevier.com/locate/apcatb

Influence of catalyst supports on H_2-SCR catalysts: A combined experimental and modeling approach including mass transfer

Andres F. Suarez-Corredor [a,b,*], Jieling Shao [a], Björn Westerberg [b], Matthäus U. Bäbler [c], Louise Olsson [a]

[a] Competence Centre for Catalysis, Chalmers University of Technology, Gothenburg, 412 96, Sweden
[b] Scania CV AB, Södertälje, 151 87, Sweden
[c] Department of Chemical Engineering, KTH Royal Institute of Technology, Stockholm, 100 44, Sweden

ARTICLE INFO

Dataset link: Pd-based H2-SCR catalytic performance test on monoliths (Original data)

Keywords:
Kinetic modeling
NO_x reduction by H_2
Pd catalyst
H_2-SCR

ABSTRACT

NO selective reduction by H_2 (H_2-SCR) has been developed as a promising technology for the emission control for H_2 combustion engines. This work focused on experimentally evaluating the effect of catalyst supports by performing material characterization, followed by the development of a kinetic model that incorporated mass transfer effects. 1 wt% Pd catalysts supported on Al_2O_3, TiO_2, BEA zeolite, and SSZ-13 zeolite were prepared and H_2-SCR performance tests were performed across the temperature range of 100–300 °C, under varying H_2/NO ratios and both dry and wet conditions. The Pd/TiO_2 sample was found to exhibit the highest performance for NO conversion and N_2 yield. Material characterization confirmed its larger Pd particle size and lower dispersion helped suppress the competing H_2 oxidation reaction; the presence of reduced-state Pd promoted catalytic conversion; and the Pd/TiO_2 chemical properties facilitated hydrogen spillover. In the kinetic model, reactions involving NO reduction to N_2, N_2O, and NH_3, as well as H_2 oxidation, were simulated, accurately reproducing the experimental trend and values for all the samples. NH_3 formation was observed only on the Pd/TiO_2-supported catalyst and was found to be independent of NO concentration. The kinetic parameters for the different samples were consistent with both the catalytic performance and material characterization results. Moreover, the study showed that external mass transfer played a crucial role by suppressing the fast hydrogen oxidation reaction, thus enhancing hydrogen availability for NO reduction.

1. Introduction

The transition towards a decarbonized transportation sector is increasingly focusing on hydrogen as a clean alternative fuel for combustion engines. [1–3]. Hydrogen combustion engines emit no CO_2, but NO_x emissions are a concern due to high combustion temperatures. Therefore, emission after-treatment strategies, which deal with hydrogen slip and NO_x reduction are essential to meet stringent emission regulations in hydrogen-powered vehicles. Hydrogen selective catalytic reduction (H_2-SCR) of NO_x using hydrogen as the reductant has emerged as a promising alternative to urea-based SCR systems. The use of hydrogen removes the need for urea injection and enables NO_x conversion at lower temperatures than conventional NH_3-SCR systems [1,2,4]. Nevertheless, one of the major challenges in H_2-SCR is achieving high selectivity towards nitrogen gas (N_2) formation while minimizing the production of nitrous oxide (N_2O), a potent greenhouse gas with a global warming potential approximately 300 times greater than CO_2 [3,5,6]. Low selectivity towards N_2 reduces the environmental benefits of hydrogen combustion and increases the complexity of the catalyst, highlighting the need for a fundamental understanding of the H_2-SCR catalytic mechanism and factors influencing selectivity.

H_2-SCR catalysts currently under development are based on Pd or Pt as active metals. [7–9]. Generally, Pd supported on metal oxides exhibits two main reaction mechanisms with two distinct temperature regions of activity: at low temperatures (100–150 °C), direct NO dissociation occurs on metallic or reduced Pd sites, while at intermediate temperatures (180–250 °C), NH_3 can also form, which thereafter can undergo classical NH_3-SCR reaction [4,10,11]. A similar pattern is observed for Pt which shows higher NO_x reduction activity at low temperatures, albeit with lower selectivity and thus higher concentrations of undesired by-products such as nitrous oxide (N_2O) [5,8,11–13].

Mechanistic studies, including In-situ Diffuse Reflectance Infrared Fourier Transform Spectroscopy (DRIFTS) and Density Functional Theory (DFT) calculations, provided further insights into the reactions.

* Corresponding author at: Competence Centre for Catalysis, Chalmers University of Technology, Gothenburg, 412 96, Sweden.
E-mail address: afelipe@chalmers.se (A.F. Suarez-Corredor).

https://doi.org/10.1016/j.apcatb.2026.126855
Received 14 November 2025; Received in revised form 17 April 2026; Accepted 22 April 2026
Available online 28 April 2026

Studies showed that NO reduction over Pd and Pt catalysts proceeds via bifunctional reaction mechanism. NO adsorption and dissociation occur predominantly on the metallic sites, creating nitrogen and oxygen atoms. Hydrogen atoms, activated on the metal surface, reduce these species, producing NH_3 at intermediate temperatures and N_2 at higher temperatures [4–6]. The support provides acidic sites for NH_4^+ ion formation and storage, facilitating the NH_3-SCR mechanism. Hydrogen spillover from metal to support enhances these processes by increasing the availability of reactive hydrogen species beyond the metal particles [2,8].

In addition to the active metal, the catalytic behavior of an H_2-SCR catalyst is also heavily influenced by the type of support, which not only disperses the metal but also modulates the electronic structure and oxidation state of the active sites through metal-support interactions [8]. Supports such as aluminum oxide (Al_2O_3), titanium oxide (TiO_2), lanthanum cobaltite ($LaCoO_3$), and various zeolites (e.g., SSZ-13, ZSM-5, SAPO-34) play multiple roles in the reaction mechanism for NO_x reduction by hydrogen [2,14]. For instance, TiO_2 supports are known to promote the reduction of Pd species to their metallic state more easily than Al_2O_3, due to strong metal-support interactions (SMSI) [15]. In addition, Al_2O_3 is also known to form stable palladium aluminates, which impacts H_2-SCR negatively [12,16]. The benefit of Pd reduction on TiO_2 enhances hydrogen dissociation, a key step in NO reduction, and increases hydrogen spillover into the support. Hydrogen spillover, i.e. the migration of activated hydrogen atoms from the metal to the support surface, is crucial for the hydrogenation of adsorbed nitrogen oxides and the formation of NH_4^+ ions on Brønsted acid sites, which subsequently participate in the NH_3-SCR cycle [14,15,17].

Compared to metal oxides, zeolite supports (particularly those with strong Brønsted acidity and thermal stability) offer an additional advantage of stabilizing ammonium ions (NH_4^+) and NH_3 intermediates formed during the hydrogenation reaction of nitrogen atoms, thus facilitating NO_x reduction through established NH_3-SCR reaction pathways [3,4,10]. The acidity strength and density of Brønsted sites directly affect NH_4^+ ion stability and mobility, thereby influencing the selectivity and overall reaction kinetics. However, excessively strong acid sites can over-stabilize NH_4^+ ions, reducing their reactivity and decreasing NO_x conversion. The ion-exchange capacity of zeolites also enables higher dispersion and incorporation of Pd ions into the framework, which can enhance NO adsorption and hydrogenation steps [3,10].

Besides the support properties, Pd particle size is also expected to influence H_2-SCR performance and selectivity, because it defines the balance between the PdO sites for NO adsorption, the reduced Pd^0 sites for H_2 activation and the metal-support interface where spillover and intermediates storage happen [18,19]. Generally, smaller particles with a larger metal-support interface facilitate H_2 spillover. This could enhance H_2 oxidation depending on the support properties [18]. Furthermore, large particles could facilitate H_2O dissociation on Pd sites, which create hydrogen reservoirs on the Pd particle which are easy to access to the adsorbed NO_x species [20].

Water vapor and oxygen, which are present at high concentrations in the exhaust gas, affect the H_2-SCR catalysts in multiple ways. Water vapor can inhibit NO conversion by competitive adsorption on active sites and blocking NO or hydrogen adsorption, particularly on Pd/Al_2O_3 catalysts [2,3,11,13]. However, it has been proposed that water can also dissociate on metal sites, increasing hydrogen coverage and potentially enhancing the hydrogenation steps when there is availability of Brønsted acid sites and high temperatures (> 180°C) [12]. Generally, the influence of water is highly dependent on the metal-support system and reaction conditions [8,10]. The role of oxygen appears comparably complex. Oxygen easily reacts with hydrogen, reducing the available H_2 to be involved in the H_2-SCR reaction. Oxygen competes with hydrogen and NO for adsorption sites. However, at low temperatures, as H_2 adsorption is the rate-limiting step, the high reactivity between oxygen and hydrogen, enhances the removal of adsorbed species, which creates vacant sites for NO and reduces N_2O formation [2,13,16].

Selectivity control remains a key challenge in H_2-SCR catalysts, with the formation of N_2O being a major concern due to its potent greenhouse gas effect. N_2O production is influenced by the coverage and ratios of adsorbed NO, N, and H species on the catalyst surface, with increased hydrogen concentrations favoring ammonia formation but sometimes promoting N_2O under certain conditions [6,14]. Pre-reduction treatments and the use of reducible supports such as TiO_2 and V_2O_5-modified catalysts have demonstrated improved N_2 selectivity and resistance to deactivation, especially in the presence of high water concentrations [2,8].

Despite the increasing interest in H_2-SCR catalysts, very little work has been devoted to their kinetic modeling. Previous studies have mainly addressed H_2-NO reactions under rich conditions, such as ammonia generation over Pt-based catalysts for passive ammonia SCR catalysis or rich phase in lean NO_x traps applications [21–23]. One study explored Pt/boron-doped graphene catalyst for H_2-SCR applications in rich conditions (without oxygen), but only presented a parity plot without a mechanistic interpretation [24]. However, the high concentration of O_2 in H_2-SCR catalysts significantly changes the reaction pathways and mechanisms, limiting the relevance of these models. As far as we can tell from the available literature, there is only one published paper reporting a kinetic model for an H_2-SCR catalyst under lean conditions, developed for a $Pt/WO_3/ZrO_2$ catalyst in dry conditions using NO, H_2 and O_2 [25]. A summary of the main kinetic parameters from these studies is presented in Table 1. The broad range in the different parameters demonstrates the dependency of them on modeled reaction mechanisms, sample properties, and experimental conditions.

To our knowledge, no kinetic models exist for H_2-SCR catalysts in lean conditions over palladium-based catalysts that focus on the role of water or account for mass transfer limitations, both of which are critical for H_2 engine applications. Kinetic models at a reactor scale are crucial for clarifying catalyst dynamics and enabling the deployment of H_2-SCR catalysts. Moreover, a systematic investigation with a kinetic model describing the role of the support has not been presented, despite its central importance in governing conversion and selectivity. Support–metal interactions can promote different reaction pathways and, under different reacting conditions, affect selectivity and reaction rates.

This study provides a comprehensive framework to address these gaps. We systematically investigate Pd supported on TiO_2, Al_2O_3, BEA zeolite and SSZ-13 zeolite. The experiments are performed on lean conditions, both in the absence and presence of water. Catalyst samples were characterized using BET surface area measurements, CO chemisorption, and X-ray photoelectron spectroscopy (XPS) to understand how support properties influence NO conversion and N_2 selectivity. Catalytic performance was evaluated for all the supports in a gas flow reactor for monolith samples under varying H_2/NO ratios and water concentrations, considering a wide experimental region. This study, performed on monoliths, reduces the confounding factors commonly present in cross-study comparisons (e.g., differences in Pd loading, preparation, and test protocols), while being relevant to aftertreatment systems. Building on these results, we develop support-specific kinetic models that identify the dominant reaction steps and capture the influence of water, the interplay of support properties, and the role of external mass transfer phenomena.

2. Methodology

2.1. Catalyst preparation and characterization

Beta zeolite (CP814E, SAR=25, powder), titanium oxide (pellets) and γ-alumina (SBa-200, powder) from Zeolyst, Thermo Scientific and Sasol, respectively, were calcined in form of powder (TiO_2 was powdered) at 550 °C for 6 h before being used as catalyst supports.

Table 1
Pt-based catalyst kinetic parameters from different studies. [21–27].

	Activation energy, E_a (kJ/mol)	NO reaction order	H_2 reaction order
NO reduction	38[24], 153[27]	0.15[24], 1[21,22]	0.7[24], 1.22[25]
N_2O formation	43[22,23], 92[21]	1[27]	1[27]
NH_3 formation	78[22,23], 131[21]	1[21,23]	1[21,23]
H_2 oxidation	44[26], 61[25]	–	1[26]

Na-SSZ-13 zeolite (SAR = 20) was synthesized in the laboratory using the hydrothermal method described earlier [28]. The Na-SSZ-13 powder was ion-exchanged to H-SSZ-13 using NH_4NO_3 (Thermo Scientific) solution twice, followed by washing with MilliQ water five times. The NH_4-SSZ-13 was then calcined at 550 °C for 6 h to transform it to H-SSZ-13. 1 wt% Pd was loaded on the four types of support materials (Al_2O_3, TiO_2, BEA and H-SSZ-13) via incipient wetness impregnation technique, using $Pd(NO_3)_2$ (Alfa Aesar 10% Pd) as the precursor. After the loading process, the wet powder was first dried at 80 °C for 12 h, followed by calcination at 600 °C for 8 h. The synthesized catalyst powder was further wash-coated on the honeycomb monoliths (Cordierite, $D \times L$ = 2.1 cm×2.0 cm, 400 cpsi) to reach a washcoat loading of 500 ± 5 mg per monolith sample. The wash-coating slurry was prepared as a solution with 50 wt% ethanol and 50 wt% Milli-Q water with a 5 wt% boehmite binder (Disperal P2, Sasol). The bare monolith was first immersed in the slurry and then it was dried with a heating gun, this process repeated 4 times. The monolith sample was dried at 80 °C for 12 h and calcined at 500 °C for 2 h.

The catalysts in powder form were characterized using multiple methods. Prior to each characterization experiment, the powder was pretreated under an oxidative atmosphere (10%O_2, 5%H_2O in Ar at 500 °C for 4 h). The Pd content was determined by Inductively coupled plasma sector field mass spectrometry (ICP-SEMS) by ALS Scandinavia (Lulea, Sweden). N_2 physisorption (Micromeritics TristarII 3000 Analyzer) measurements provided surface areas and pore volumes (BET and t-plot methods), and X-ray diffraction (XRD) was used to evaluate the crystalline structure of the samples using a D8 advanced diffractometer (Bruker AKS, CuKα radiation). CO chemisorption was done to measure metal dispersion (Micromeritics ASAP2020 Plus). High-resolution transmission electron microscopy (HRTEM) was performed to visualize the particle morphology and distribution (FEI Titan 80–300 microscope). X-ray photoelectron spectroscopy (XPS) analysis was employed to study oxidation states (PHI5000 VersaProbe III-Scanning XPS™), and Temperature-programmed desorption of ammonia (NH_3-TPD) was used to evaluate the acidity of the support (Sensys DSC calorimeter, Setaram). Detailed experimental details of each characterization technique are given in the Supporting Information, section S1.

2.2. Catalyst performance test

Catalyst performance tests were performed in a gas flow reactor for monolith samples. The gas flow reactor consists of three sections: a flow control section equipped with several mass flow controllers (MFCs); the reactor section with the sample holder located in a temperature controlled zone; and the gas analysis section with a Fourier transform infrared (FTIR) spectroscopy equipment (AVL Sesam i60FT) and a O_2 sensor (AVL Magnos 106). A detailed description of the setup is given in [29] (see also Fig. S1 in Supporting Information). Two monoliths, each 2 cm in length, were placed in row in the reactor. For H_2 estimation, the water signal from the FTIR at dry experiment conditions was used. When water was added, the signal from the FTIR has high noise and the discrimination between H_2O from the feed and H_2O formed in the reaction was not possible.

The reference temperature for the kinetic model and analysis was assigned to the sample inlet. Temperature variation along the sample at steady state were around $3 - 10$°C. Each sample was subject to pretreatment procedure to stabilize the catalyst at an oxidized state. In the pretreatment, the sample was heated to 500 °C, with a constant gas flow of 15 NL/min and a gas composition of 5% H_2O and 10% O_2. The flow represents a space velocity of 65000 h^{-1}. After the pretreatment, the performance test was started. For all the experiments, the carrier gas in the gas flow reactor was nitrogen.

The performance tests aimed at measuring the catalytic performance of the four catalyst samples at different temperatures and gas compositions. In the test, the temperature was set to the experiment temperature, and it was stabilized, using nitrogen only, until isothermal conditions were reached. Then, the water and oxygen concentration were set until it was stable. For all the experiments, the oxygen concentration was set to 10% and NO to 500 ppm. Experiments with different water concentrations, 0%, 5% and 10%, were used to study the effect of water. When the water and oxygen concentration was constant, different steps, changing the H_2 concentration (7500, 5000, followed by 2500 ppm) were performed, corresponding to H_2/NO ratios of 15, 10, and 5, respectively, and each step was held until steady-state conditions were reached. Eight temperatures were studied, chosen from an earlier screening procedure done examining H_2-SCR performance. The test temperature ranges from 100 to 300 °C. The detailed experiment scheme is presented in the Supporting Information, Fig. S2.

2.3. Catalyst model development

The catalyst model treats the gas flow reactor as a diluted, isothermal and radially homogeneous plug flow reactor. Six chemical species are considered. On one hand, these are the limiting reactants NO and H_2 and the products N_2O and NH_3 whose concentrations evolve along the length of the catalyst sample. On the other hand, the reactants O_2 and H_2O are present in excess and, accordingly, their concentration variation along the catalyst is negligible, due to their high concentrations. NO_2 was not detected in the experiments and therefore not included in the model. The six species distribute between the bulk gas phase and the catalyst washcoat. Steady state mass balances for the limiting reactants and the products read as:

$$v\frac{d\bar{c}_i}{dz} = \sum_j \nu_{i,j} r_j(C_{NO}, C_{H_2}; C_{O_2}, C_{H_2O}), \quad i = NO, H_2, N_2O, NH_3 \tag{1}$$

where $\bar{c}_i$ and C_i are the concentration of species i in the bulk gas phase and the catalyst washcoat, respectively, v is the superficial gas flow velocity (which due the diluted conditions is treated as a constant), z is the axial coordinate, $\nu_{i,j}$ is the stoichiometric coefficient of species i in reaction j, and r_j is the reaction rate in reaction j. The left hand side of Eq. (1) describes convective transport of species i in the gas phase, while the right-hand-side describes the formation of species i in the washcoat. Consequently, the reaction rate r_i depends on the reactant concentrations in the washcoat. Mass transfer between the gas phase and the catalyst washcoat is described by means of a mass transfer coefficient $k_{m,i}$:

$$a_p k_{m,i}(\bar{c}_i - C_i) = -\sum_j \nu_{i,j} r_j(C_{NO}, C_{H_2}; C_{O_2}, C_{H_2O}) \tag{2}$$

where $a_p = 4d_o/d_c^2$ is the washcoat surface area per unit volume of monolith, with d_o denoting the open channel width and d_c the honeycomb channel width (open channel plus twice the washcoat thickness).

The geometrical characteristics of the monolith channel are described in Fig. S3 in the Supporting Information. The mass transfer coefficient $k_{m,i}$ is calculated from a Sherwood correlation as described below. Eqs. (1) and (2) are complemented with models for the reaction rates r_i whose development based on data from the experiments is presented in the result section.

Mass transfer limitations. For assessing the mass transfer limitations we considered a reduced model that ignores mass transfer and that only accounts for the consumption of NO and H_2. The reduced model thus consisted of Eqs. (1) written for i = NO and H_2, and $\bar{c}_i$ replaced by C_i. Fitting this reduced model to the experimental data allowed for determining the apparent reaction rates for NO and H_2, denoted by $r_{\mathrm{NO}}^{\mathrm{obs}}$ and $r_{\mathrm{H_2}}^{\mathrm{obs}}$.

External mass transfer was assessed by calculating the Damkohler number that relates the reaction rate to the external mass transfer rate. In the present case, Damkohler number is defined as:

$$Da_i = \frac{r_i^{\mathrm{obs}}}{a_p k_{m,i} \bar{c}_i} \tag{3}$$

where $k_{m,i}$ is the external mass transfer coefficient of species i. The latter was estimated using the Sherwood correlation for monolith catalysts with square channels [30]:

$$Sh = Sh_a + 6.874(1000 z_{Sh})^{-0.488} \exp(-57.2 z_{Sh}) \tag{4}$$

where $Sh = k_{m,i} d_o / D_i$ is the Sherwood number, with D_i being the molecular diffusivity; Sh_a is the asymptotic Sherwood number which for square channels assumes $Sh_a = 3$; and $z_{Sh} = zD_i/(\upsilon d_o^2)$ is the dimensionless axial coordinate. The molecular diffusivity was calculated using the Wilke's mixture equation with the binary diffusion activities obtained from the Fuller–Schetter–Giddings equation [31]. For $Da > 10$, external mass transfer dominates and significantly affects the overall conversion rate, whereas for $Da < 1$, the reactor operates in the kinetic regime where the reaction kinetics govern the overall conversion rate.

Internal mass transfer was assessed by calculating the Weisz–Prater criterion which compares the overall reaction rate and the internal mass transfer in the porous washcoat. The Weisz–Prater criterion is defined as:

$$N_{WP,i} = \frac{r_i^{\mathrm{obs}} d_a^2}{D_{\mathrm{eff},i} C_i} \tag{5}$$

where d_a is the washcoat thickness and $D_{\mathrm{eff},i}$ is the effective diffusivity of species i in the porous washcoat. The latter is calculated from the combination of molecular diffusion (D_i) and Knudsen diffusion ($D_{k,i}$):

$$D_{\mathrm{eff},i} = \frac{\epsilon/\tau}{D_i^{-1} + D_{k,i}^{-1}} \tag{6}$$

where ϵ is the washcoat porosity and τ is its tortuosity. The former was estimated from measurements of the pore volume from the N_2 physisorption experiment and the washcoat density, while the tortuosity was assumed to be 3, from previous studies [32–34]. The Knudsen diffusivity $D_{k,i}$ was calculated as described by Thomas et al. [35]. Additional parameters can be found in Supplementary Information, section S4.

Parameter optimization. The catalyst model was implemented in MatLab and solved using *ode15s*. For this, the governing Eqs. (1) and (2) were rewritten in dimensionless form to simplify numerical integration. Initial conditions to Eq. (1) were taken as the reactor inlet gas composition. The reactor model was coupled to an optimization module for estimating the kinetic parameters by minimizing the difference between the experimental concentrations at the reactor outlet and the modeled ones. The objective function was defined as the sum of the normalized squared residuals, adjusted for the number of data points for each gas phase species:

$$\min(F) = \min\left(\sum_{i=1}^{G} \frac{N_i - 1}{N_i} \sum_{j=1}^{N_i} \frac{(y_{i,j}^{exp} - y_{i,j}^{mod})^2}{\sigma_i^2} \right) \tag{7}$$

where $G = [\mathrm{NO}, \mathrm{H_2}, \mathrm{N_2O}, \mathrm{NH_3}]$ is the number of detected gas species, N_i is the number of datapoints for species i, $y_{i,j}$ is the mole fraction concentration of species i in experiment j, and σ_i^2 is the variance of all concentration measurements of species i. The objective function given in Eq. (7) integrates over all species and all experiments, thus providing a balanced contribution of all the fitted data which enhances information use, facilitates convergence, and reduces issues of parameter correlation in complex optimization tasks [36]. Thereby, the adjustment by the number of datapoints, i.e. the term $(N_i - 1)/N_i$ in Eq. (7), is important to weigh the contribution for species for which less data was available. This is in particular the case for H_2 whose experimental concentration was derived from product water and thus was only available under dry conditions.

The optimization workflow was carried out using a genetic algorithm with a high mutation rate to map the objective function over the parameter ranges. A high mutation ratio ensures an efficient mapping of the objective function in the optimization region. Then a refinement with external mass transfer and a narrowed experimental region was done, finalized with a fine optimization of the five best parameter sets using a gradient method (lsqnonlin). A scheme of the optimization workflow is given in the Supporting Information, Fig. S4.

The model quality was evaluated by indicators such as the adjusted R-squared, the Akaike Information criteria (AIC), and the residual distribution of the model. Also, the correlation matrix and parameter confidence intervals were calculated to assess overfitting of the model. Although the adjusted R-squared is not strictly designed for non-linear models, it is a useful and intuitive measure of overall model performance, which is recommended to complement by other indicators better suited to non-linear models [37,38]. Additional indicators used for model quality are described in more detail in section S3 in the Supporting Information [39,40].

3. Results and discussion

3.1. Catalyst characterization

The physical properties of the four catalyst samples are shown in Table 2. The actual Pd loading for all four catalysts was 0.8–0.9 wt% which is slightly lower than the calculated 1 wt%. Furthermore, the specific surface area for the zeolite-supported catalysts Pd/BEA and Pd/SSZ-13 was found to be higher than that of the oxide-supported ones (526 and 614 m^2/g compared to 170 and 31 m^2/g for Pd/Al_2O_3 and Pd/TiO_2, respectively) which is well known and reflects the morphology and framework of zeolites [42]. Accordingly, the zeolite-supported catalysts exhibit small palladium particle sizes and high dispersion as determined through CO chemisorption measurements.

The dispersion ratio decreased according to Pd/SSZ-13 > Pd/BEA > Pd/Al_2O_3. The mean particle size followed the opposite trend (see Table 2). Regarding the Pd/TiO_2 sample, CO chemisorption was revealed to be an unsuitable technique for this catalyst due to the reducibility of TiO_2 and *strong metal-support interaction* (SMSI) effects [43]. SMSI effects involve an enrichment of the metal surface by partially reducible metal oxides, facilitating electron transfer between the support and the metal [44–46]. Since there is a reduction pretreatment with H_2 at 400 °C before the CO adsorption, the CO chemisorption was suppressed as a result. To evaluate the particle size and dispersion of the Pd/TiO_2 catalyst, we therefore reverted to the analysis of TEM images. Approximately 100 randomly selected particles were measured to derive the particle size distribution and plot a histogram as shown in Fig. 1. To validate this method, TEM images were also taken for Pd/Al_2O_3. The mean particle size obtained from TEM images of Pd/Al_2O_3 is about 4.3 nm, which is consistent with the result from CO chemisorption measurements (4.4 nm). Compared to this, the TEM images of Pd/TiO_2 gave a larger mean particle size of around 16.6 nm. Therefore, combining the CO chemisorption and TEM results (Fig. 1 and Fig. S5), the particle

Table 2
Physical properties catalyst samples.

	Pd loading (mg/kg)	Surface area (m^2/g)	Pore volume (cm^3/g)	Dispersion (%)	Mean particle size (nm)
Pd/Al_2O_3	0.87	170.1	0.43	25.5	4.4
Pd/TiO_2	0.88	30.9	0.13	7.0[a]	16.6[a]
Pd/BEA	0.93	526.0	0.66	48.9	2.3
Pd/SSZ-13	0.80	613.8	0.43	64.4	1.7

[a] The particle size of Pd/TiO_2 was measured and calculated from TEM images. The dispersion of Pd/TiO_2 was calculated based on [41]. Other dispersion and mean particle size results were obtained by CO chemisorption measurements.

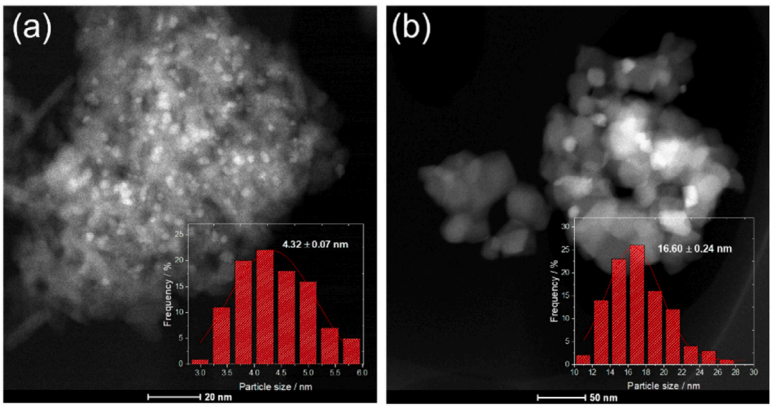

Fig. 1. HAADF-HRTEM images of (a) Pd/Al_2O_3 and (b) Pd/TiO_2 catalysts and the particle size distributions.

Table 3
X-ray photoelectron spectroscopy results of Pd catalysts.

	Pd^0		Pd^{2+}		Pd^{4+}	
	BE/eV ($Pd3d_{5/2}/3d_{3/2}$)	Fraction %	BE/eV ($Pd3d_{5/2}/3d_{3/2}$)	Fraction %	BE/eV ($Pd3d_{5/2}/3d_{3/2}$)	Fraction %
Pd/Al_2O_3			336.7/342.1	54.8	337.9/343.3	45.2
Pd/TiO_2	335.3/340.6	31.8	336.7/342.0	68.2		
Pd/BEA			336.5/341.7	32.0	338.0/343.3	68.0
Pd/SSZ-13			336.0/341.3	7.4	338.0/343.4	92.6

sizes of the four catalysts are in the order from small to large Pd/SSZ-13 < Pd/BEA < Pd/Al_2O_3 < Pd/TiO_2.

The XRD patterns of the four catalysts are shown in Fig. S6 in Supporting Information. All samples display the characteristic reflections of their support materials. The typical anatase patterns of TiO_2 was observed for the Pd/TiO_2 sample, while based on the reference card number from the Joint Committee on Powder Diffraction Standards (JCPDS), no distinct PdO (JCPDS: 88-2434) or Pd (JCPDS: 87-0645) was detected, likely due to the low loading and small particle size on the surface [47]. For the zeolite catalysts Pd/BEA and Pd/SSZ-13 the reflections of PdO (002) and (101) surfaces and Pd (111) surfaces overlap with the reflections of the zeolite framework.

The oxidation state of Pd in the four catalyst samples was examined using XPS. Results are shown in Fig. 2 and Table 3. Fig. 2 shows the deconvoluted Pd 3d spectra of the four catalyst samples. The characteristic reflections of the Pd $3d_{5/2}$ spectra at 336.0–337.0 eV and 337.9–338.0 eV correspond to Pd^{2+} and Pd^{4+} species, respectively [48–50]. According to Moulder's handbook [51], the reflections belonging to the Pd $3d_{3/2}$ spectra have a fixed binding energy shift of +5.26 eV with respect to Pd $3d_{5/2}$ which is clearly observed in all four panels in Fig. 2. Observing Pd^{2+} and Pd^{4+} species in the catalyst samples can be explained by noticing that the catalysts underwent hydrothermal treatment in an oxidative environment during degreening. Palladium in all catalysts, except Pd/TiO_2, is thus present in the oxidized state. For Pd/TiO_2, the Pd $3d_{5/2}$ spectra displays reflections at binding energies of 335.0–335.5 eV and 336.7 eV, which are assigned to metallic Pd (indicated as Pd^0 in Fig. 2, upper-right panel) and Pd^{2+}, respectively. The presence of metallic Pd in Pd/TiO_2 might indicate an SMSI effect that facilitates electron transfer between the support and the metal and causes an electron enrichment on Pd [52]. We also observed that after being stored for more than one year, this catalyst powder still retained metallic Pd, but to a smaller extent. Table 3 summarizes the results of the XPS analysis. Putting aside Pd/TiO_2, the fraction of Pd^{2+} is order from low to high Pd/SSZ-13 < Pd/BEA < Pd/Al_2O_3. The fraction of Pd^{4+} increases in opposite order. It is noted that the XPS measurement is a surface technique, and the oxidation states calculated by deconvolution are semi-quantitative. The spectra of zeolite catalysts exhibit pronounced noise, which is attributed to the low metal dispersion on the surface.

The four catalyst samples were subject to NH_3-temperature programmed desorption (TPD) measurements, to get an insight into the adsorption capacity and nature of acid sites. The TPD curves (shown in Fig. S7 in Supporting Information) in most cases showed two peaks, one at around 210±5°C and one at around 420±5°C representing weak and strong acid sites, respectively. Desorption of NH_3 from strong acid sites at over 400 °C is typically associated to Brønsted acid sites, while peaks at 100-300 °C are associated to Lewis acid sites [53]. The two zeolite catalyst Pd/BEA and Pd/SSZ-13 exhibit a larger adsorption capacity compared to the two metal oxide catalyst Pd/Al_2O_3 and Pd/TiO_2, with Pd/BEA having more weak acid sites and Pd/SSZ-13 having more strong acid sites. The adsorption capacity of the two metal oxide catalysts is relatively small, with Pd/TiO_2 having virtually no strong adsorption sites. The acidity of the catalyst, which is mainly controlled by the catalyst support, plays a significant role in determining the chemical state of noble metals [54,55].

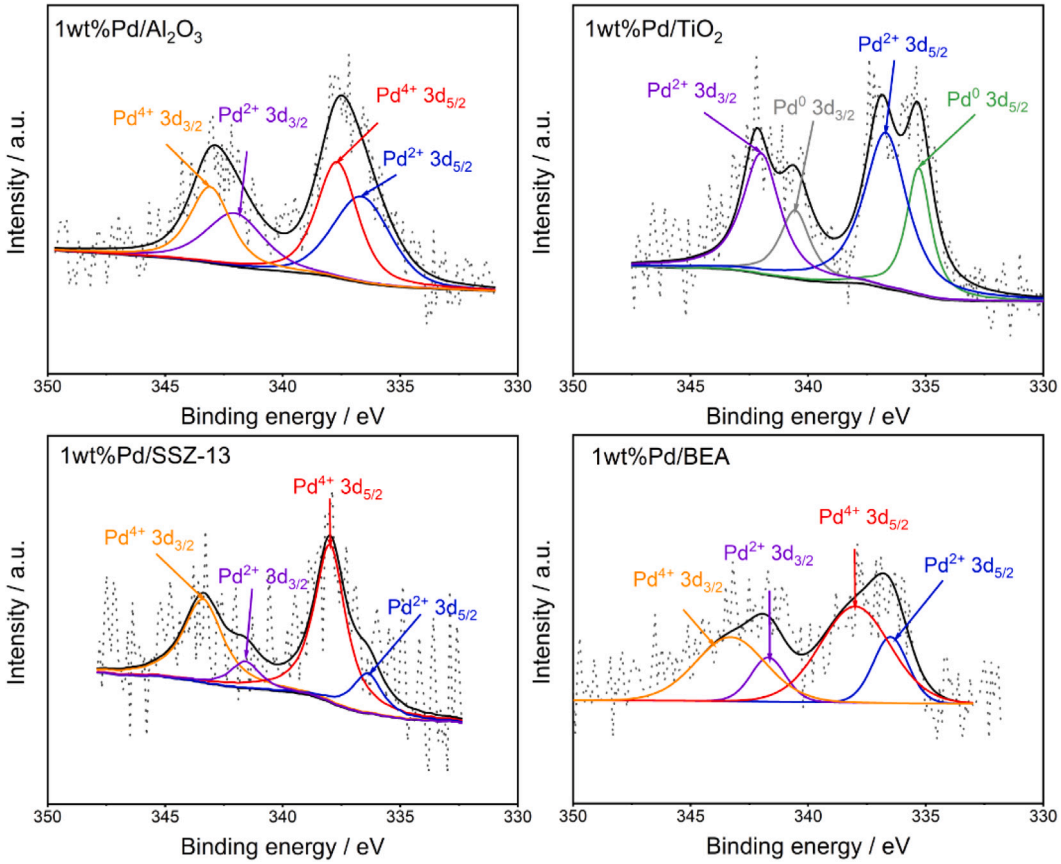

Fig. 2. X-ray photoelectron spectra of pretreated 1 wt% Pd catalysts supported on Al_2O_3, TiO_2, SSZ-13 and BEA. Black dashed line: raw spectra. Black solid line: pre-processed spectra for deconvolution.

3.2. Catalytic performance

The catalytic performance of the four catalyst samples was investigated by measuring NO conversion in a flow reactor at different H_2/NO ratios, water concentrations, and temperatures. Fig. 3 shows the NO conversion as a function of temperature for all four catalyst samples, organized by water concentration (rows) and H_2/NO ratio (columns). From the experimental data obtained in the catalytic performance tests, NO conversion was calculated as follows:

$$X_{NO} = \frac{y_{NO}^{in} - y_{NO}^{out}}{y_{NO}^{in}} \tag{8}$$

where y_{NO}^{in} is the mole fraction of NO at the reactor inlet, and y_{NO}^{out} is the mole fraction of NO at the reactor outlet. Among the four catalyst, Pd/TiO_2 exhibited the highest NO conversion across every H_2/NO ratio and water content. Under dry conditions, its conversion peaked at 180 °C. When water was introduced, the peak shifted slightly to higher temperatures, between 180 and 200 °C. Pd/Al_2O_3 followed a similar trend, although with lower conversion values than Pd/TiO_2. Its highest conversion occurred under dry conditions at 180 °C and the conversion window becomes broader with increasing the H_2/NO ratio. Pd/BEA exhibited with the highest conversion at low temperatures (100–130 °C), achieving about 50% NO conversion under dry conditions at a H_2/NO ratio of 15. However, this low-temperature peak disappeared when water was added, shifting the conversion to higher temperatures and lower values. Pd/SSZ-13 showed the lowest overall conversion across most conditions. Under dry conditions, the conversion for this catalyst had its maximum at 150 °C, while under wet conditions the peak diminished and shifted to 200 °C.

The most significant conversion gain came from increasing the H_2/NO ratio from 5 to 10. Further increase of H_2/NO gave only small benefits for most catalysts. Notable exception were Pd/BEA which showed a distinct conversion rise at low temperatures (around 130 °C), and Pd/TiO_2 which showed an increase from 40% to 50% when increasing the H_2/NO ratio from 10 to 15 at 10% water concentration. Overall, higher H_2/NO ratios improved NO conversion under both dry and wet conditions, with stronger enhancements observed when no water was present. The positive impact of higher H_2/NO was most evident for Pd/Al_2O_3 and Pd/TiO_2. The presence of water, on the other hand, consistently reduced NO conversion across all catalyst samples. The degree of inhibition followed the order, from most inhibited to least inhibited Pd/BEA > Pd/Al_2O_3 > Pd/SSZ-13 > Pd/TiO_2. Water also delayed the NO light-off temperature towards higher values in all cases.

At temperatures above 250 °C, all catalysts showed low conversion, regardless of water content or H_2/NO ratio. This behavior is attributed to the increased rate of H_2 oxidation on palladium, which overcomes NO reduction by consuming all the available H_2. Although, the low conversion at high temperatures for all the samples could be interpreted as a thermodynamic limitation, this is not the case for the current study. NO_2 was not detected by the FTIR measurements, indicating that NO oxidation equilibrium does not constrain the observed reaction rates. The decrease on NO conversion reflects the competition between H_2 oxidation and NO reduction.

To further examine the catalytic performance, we calculated the reaction yield of NO, defined as the product of NO conversion (X_{NO}) multiplied by the selectivity towards species i (S_i), where i stands for any of the products that form in the reactions with NO. Using the reactor inlet and outlet concentrations, the reaction yield towards species i follows as:

$$Y_i = X_{NO} S_i = \frac{y_i^{out} \zeta_i}{y_{NO}^{in}}, \quad \text{for } i = N_2O, NH_3 \tag{9}$$

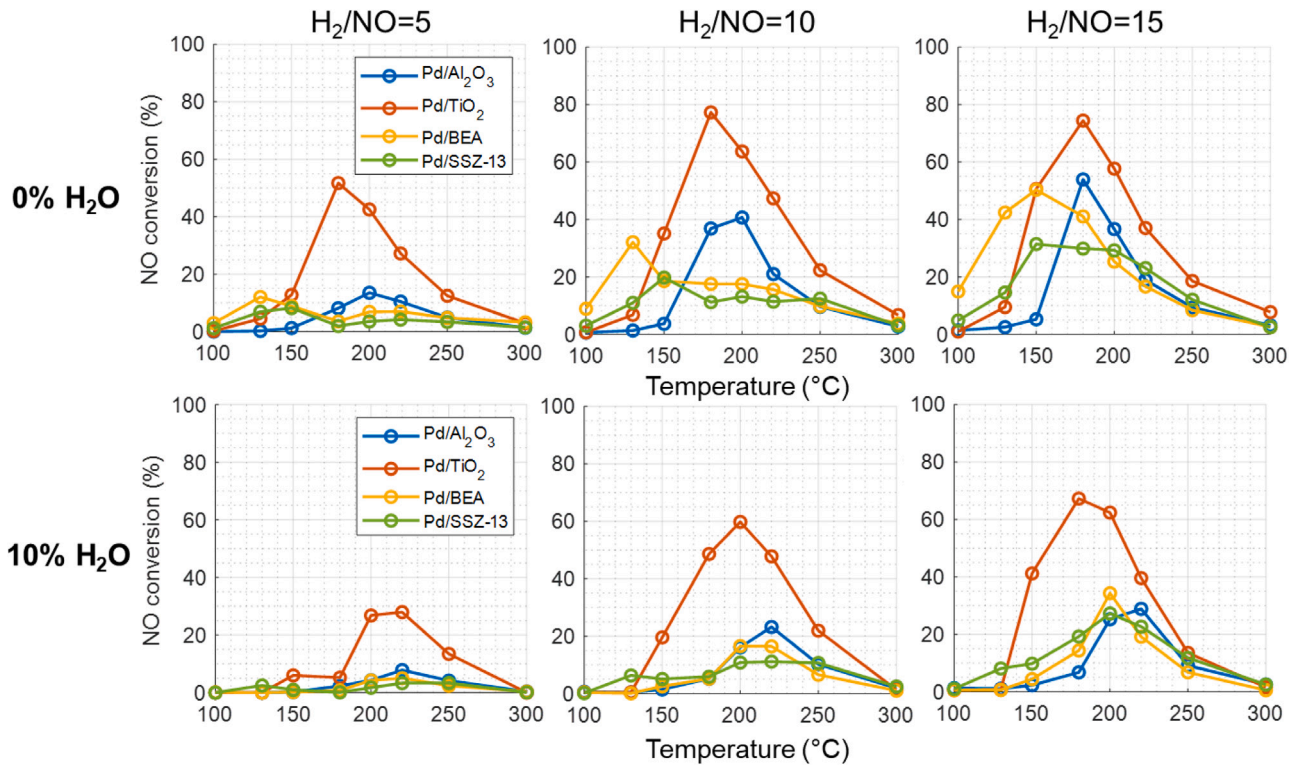

Fig. 3. NO conversion as a function of temperature for the different H_2-SCR catalysts. Rows refer to different water concentrations: 0 and 10%; Columns refer to different H_2/NO ratios: 5, 10, 15. NO concentration is 500 ppm.

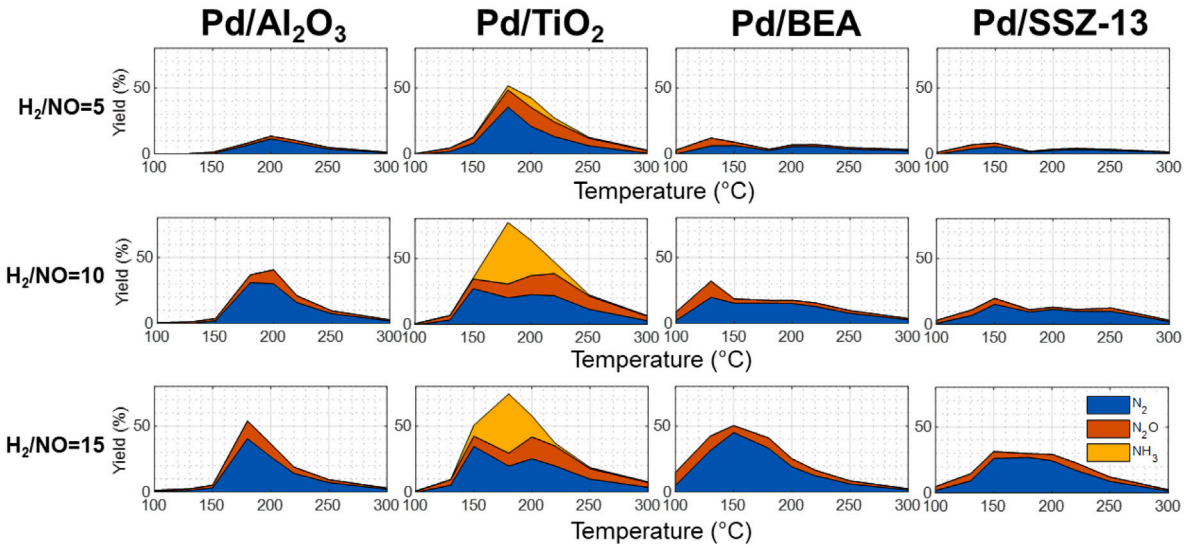

Fig. 4. Yield contour maps for all catalyst samples at dry conditions, 0% H_2O. Rows refer to different H_2/NO ratios: 5, 10 and 15. Columns refer to different catalyst samples.

where y_i^{out} is the mole fraction concentration of species i at the reactor outlet, y_{NO}^{in} is the mole fraction of NO at the reactor inlet, and ζ_i is the number of nitrogen atoms in one molecule of species i. The yield for N_2, i.e. how much of NO converted into N_2, followed from the balance $Y_{N_2} = X_{NO} - Y_{N_2O} - Y_{NH_3}$.

NO_2 was not observed under the studied conditions. According to the literature [56,57], oxidation of NO by Pd becomes relevant only temperatures above those studied here.

Fig. 4 shows the reaction yield under dry conditions as a function of temperature. Each column refers to a specific catalyst while the rows refer to different H_2/NO ratios. In each panel, the yield towards N_2, N_2O, and NH_3 is shown as a contour map. Pd/Al_2O_3 exhibited high N_2 selectivity under most conditions, but low yields due to low NO conversion. The yield increases with increasing H_2/NO ratio, with the highest value observed at 180 °C where the N_2 yield reached 40% and the N_2O yield 10%, at the highest NO conversion point. Pd/TiO_2 was the only catalyst that produced NH_3, with its yield increasing at a H_2/NO of 10 and decreasing afterward. Under dry conditions, the N_2 yield reached 30% at 180 °C and a H_2/NO ratio of 5; the N_2 yield varied only slightly at higher H_2/NO ratios. Pd/BEA achieved the highest N_2 yield, peaking at 40% at 150 °C and a H_2/NO ratio of 15. As temperature increased, the N_2O yield decreased, shifting from

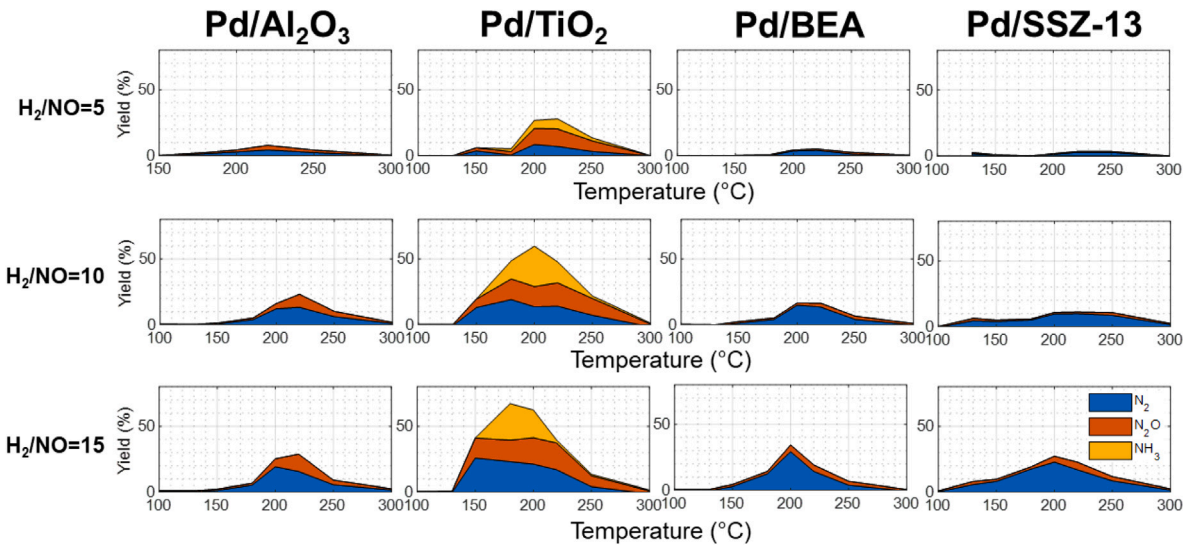

Fig. 5. Yield contour maps for all catalyst samples at 10% H_2O concentration. Rows refer to different H_2/NO ratios: 5, 10 and 15. Columns refer to different catalyst samples.

around 10% at low temperatures to less than 5% at high temperatures. Pd/SSZ-13 showed similar behavior as Pd/BEA during dry conditions.

Fig. 5 shows the yield contour maps at 10% water concentration. In general, the presence of water reduced the N_2 yield and promoted N_2O formation, especially at temperatures between 150 and 250 °C. This is most visible for Pd/Al_2O_3 for which the presence of water reduced the N_2 yield while increasing N_2O formation, particularly at high temperatures (> 200°C) and high H_2/NO ratios. For Pd/TiO_2, water had a strong impact, reducing the overall yield for N_2, NH_3 and N_2O, especially at high H_2/NO ratios. At high temperatures (> 250°C) and high water concentration, N_2O selectivity was the highest, with a drop in N_2 selectivity. Pd/BEA showed a narrowing of its high N_2 yield region under wet conditions. The highest N_2 yield was reached at 200 °C with a reduction in the formation of N_2O. At high temperatures, N_2O selectivity is high but the catalyst has the lowest yield. In contrast, Pd/SSZ-13 remained relatively stable across the different conditions when adding water. Changes in water concentration and the H_2/NO ratios had minimal effect on the selectivity profile, but influenced the overall yields. The N_2O yields was around 5% at 200 °C for Pd/SSZ-13, however, this is due to the lowest NO conversion which is reflected by the low overall yield.

3.3. Catalyst modeling

The experiments in the flow reactor revealed that the reaction between NO and H_2 on Pd/Al_2O_3, Pd/BEA, and Pd/SSZ-13 leads to the formation of N_2 and N_2O, while Pd/TiO_2 additionally lead to formation of NH_3, next to N_2 and N_2O. NO_2 was not detected, as the experimental temperature range was too low for significant NO oxidation [56,57]. Based on these observations a reaction scheme based on four stoichiometric reactions was proposed:

R1: $NO + H_2 \longrightarrow H_2O + 0.5\,N_2$ (I)

R2: $H_2 + 0.5\,O_2 \longrightarrow H_2O$ (II)

R3: $2\,NO + H_2 \longrightarrow N_2O + H_2O$ (III)

R4: $2\,NO + 5\,H_2 \longrightarrow 2\,NH_3 + 2\,H_2O$ (IV)

Reaction (I), (II), and (III) are relevant for all four catalysts as all catalysts showed formation of N_2O, N_2 (via mass balance), and hydrogen oxidation. On the other hand, Reaction (IV) is only relevant for Pd/TiO_2 as this was the only catalyst for which NH_3 was detected.

Table 4
Rate expressions for Reaction (I) to (IV).

$$r_1 = \frac{A_1 \exp\left(\frac{-E_{a,1}}{RT}\right) C_{NO}^{\alpha_1} C_{H_2}^{\alpha_2}}{1 + A_1^I \exp\left(\frac{-E_{a,1}^I}{RT}\right) C_{H_2O}^{\alpha_3}} \quad (10)$$

$$r_2 = \frac{A_2 \exp\left(\frac{-E_{a,2}}{RT}\right) C_{H_2}^{\beta_1} C_{O_2}}{1 + A_2^I \exp\left(\frac{-E_{a,2}^I}{RT}\right) C_{H_2O}^{\beta_2}} \quad (11)$$

$$r_3 = A_3 \exp\left(\frac{-E_{a,3}}{RT}\right) C_{NO}^{\delta_1} C_{H_2}^{\delta_2} \quad (12)$$

$$r_4 = \frac{A_4 \exp\left(\frac{-E_{a,4}}{RT}\right) C_{NO}^{\gamma_1} C_{H_2}^{\gamma_2}}{1 + A_4^I \exp\left(\frac{-E_{a,4}^I}{RT}\right) C_{H_2O}^{\gamma_3}} \quad (13)$$

Reaction (I) to (IV) were modeled as quasi-homogeneous reactions assuming power-law kinetics with an Arrhenius-type temperature dependency. The inhibiting effect of H_2O was accounted for by including an additional power-law expression as denominator. The empirical rate expressions for reaction (I) to (IV) are given in Table 4. In this table, A_j and $E_{a,j}$ denote the prefactor and the activation energy for reaction j, respectively, while the greek letters $\alpha_1 \ldots \beta_1 \ldots \delta_1 \ldots \gamma_1 \ldots \gamma_3$ represent empirical reaction orders. The oxygen concentration was not varied in the experiments. As a consequence, the reaction order for O_2 in Reaction (II) could not be determined and therefore was set to unity in Eq. (11). Also, formation of N_2O was found to be independent of the water concentration. Therefore, no water inhibition function was included in the rate expression Reaction (III), see Eq. (12). The power-law rate expressions in this study were not intended to represent a sequence of elementary reaction steps, which will vary with supports. Rather, they were aimed to capture the observed temperature and concentration dependencies, which can be coupled to mass transfer descriptions to provide insight into the catalyst performance in monoliths.

Mass transfer analysis. For the analysis of mass transfer limitations we first estimated the apparent reaction rates of NO and H_2 by fitting a reduced model to the experimental data. The reduced model considered only reaction (I) and (II) and ignored mass transfer limitations between the bulk gas and the washcoat, such that $\bar{c}_i = C_i$. Accordingly, the

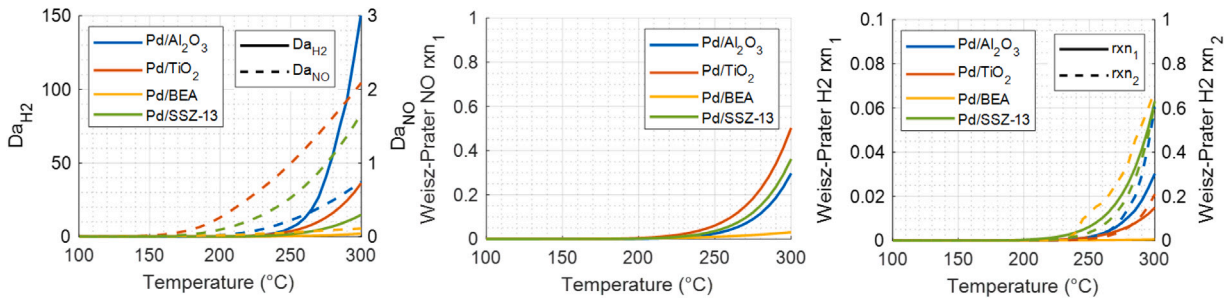

Fig. 6. Damkohler number (Da) and Weisz–Prater criterion ($N_{WP,i}$) from the apparent reaction rate r_{NO}^{obs} and $r_{H_2}^{obs}$. Left: Da for H_2 (solid line) and NO (dashed line). Middle: N_{WP} for NO. Right: N_{WP} for H_2 from reaction (I) (solid line) and reaction (II) (dashed line). The panels show the highest values of Da and $N_{WP,i}$ across the catalyst length as a function of temperature for all catalyst samples. H_2/NO = 15 (H_2 7500 ppm) and 10% H_2O.

reduced model can be written as:

$$v\frac{dC_{NO}}{dz} = -r_1, \qquad v\frac{dC_{H_2}}{dz} = -r_1 - r_2 \tag{14}$$

where r_1 and r_2 are the reactions rates of Reaction (I) and (II) given in Table 4. Fitting Eq. (14) to the experimental data resulted in the apparent reaction rates r_{NO}^{obs} and $r_{H_2}^{obs}$ which were used to calculate the Damkohler number (Da) and the Weisz–Prater criterion ($N_{WP,i}$), according to Eqs. (3) and (5).

Fig. 6 shows the Damkohler number and the Weisz–Prater criterion obtained in this way for the different catalysts under the most severe experimental conditions (H_2/NO = 15, 10% H_2O). The three panels thereby show the highest value of Da and $N_{WP,i}$ along the catalyst length as a function of the temperature. Both Da and $N_{WP,i}$ show a strong increase with temperature. However, while Da assumes values well above unity, the Weisz–Prater criterion $N_{WP,i}$ within the considered temperature range remains below unity. From the magnitude of Da and $N_{WP,i}$ we thus conclude that internal mass transfer is negligible for all catalyst samples (because $N_{WP,i} < 1$), while external mass transfer rapidly becomes relevant as the temperature increases (because $Da > 1$).

Reaction kinetics. Based on the above findings, a catalyst model that takes into account external mass was developed. The full catalyst model consists of Eqs. (1) and (2) formulated for the reactants NO and H_2 and the products N_2O and NH_3. The mass transfer coefficient appearing in Eq. (2) was calculated from the Sherwood correlation given in Eq. (4). The full catalyst model reads as:

$$v\frac{d\bar{c}_{NO}}{dz} = r_{NO} = -r_1 - 2r_3 - 2r_4 \tag{15a}$$

$$v\frac{d\bar{c}_{H_2}}{dz} = r_{H_2} = -r_1 - r_2 - r_3 - 5r_4 \tag{15b}$$

$$v\frac{d\bar{c}_{N_2O}}{dz} = r_3, \quad v\frac{d\bar{c}_{NH_3}}{dz} = 2r_4 \tag{15c}$$

$$a_p k_{m,i}(\bar{c}_i - C_i) = -\sum_j \nu_{i,j} r_j, \quad i = \mathrm{NO}, \mathrm{H_2} \tag{15d}$$

where r_1 to r_4 are the reaction rates given in Table 4 evaluated at the washcoat concentrations C_i. The catalyst model (15) was applied to the experimental data by optimizing the model parameters, using the objective function (7). Given that the Pd/TiO_2 sample showed the highest conversion, it was elected for a more in-depth analysis with modeling results shown in Fig. 7. Modeling results for the other catalyst samples can be found in Supporting Information, section S6. The modeling results in the Supporting Information present the outlet gas composition and yields. Overall, the modeled yields follow the same trends and magnitudes as the experimental data, with a slight underestimation of N_2O formation for the zeolite-based samples under dry conditions and an overestimation of N_2 formation in the 150–200 °C range under both dry and wet conditions. From Fig. 7, the model accurately predicts NO conversion as well as the formation of N_2O, NH_3, and N_2 (by nitrogen balance). A key featured captured is the maximum NO conversion at around 200 °C, followed by a decrease at higher temperatures (> 200°C), where H_2 oxidation dominates over NO reactions. The influences of water and different H_2/NO ratios was well captured, by optimizing the reaction orders and inclusion of water inhibition. N_2O and NH_3 were estimated with proper magnitude and trend, showing a maxima of formation aligned with the peak in NO conversion.

Table 5 summarizes the kinetic parameters for the full catalyst model for all catalyst samples. The activation energies for the hydrogen reactions ($E_{a,1}$, $E_{a,2}$ and $E_{a,3}$) are of similar magnitude for all catalysts, while the activation energy for the water inhibition ($E_{a,i}^{I}$) varies significantly among the different samples, suggesting different extents of water inhibition among the different catalysts. Notice that no direct comparison of the pre-exponential factors can be done, due to differences in units dictated by the reaction order. The latter were found to lie between 1 and 2. Reaction orders near 1 may indicate single-molecule surface mechanisms without adsorption limitations, whereas values around 2 could point to the involvement of more than one molecule or dissociative adsorption [35,58,59].

Fig. 8 presents the reaction orders for the four reactions for all four catalyst samples. For NO reduction (reaction (I)), Pd/TiO_2 exhibits the highest reaction order for NO and the lowest for H_2, indicating that the NO concentration strongly influences its reduction, while the role of H_2 is more limited. In contrast, Pd/BEA shows the largest H_2O inhibition order, suggesting that water has a stronger inhibitory effect on this catalyst. In the case of H_2 oxidation (reaction (II), Pd/SSZ-13 has the highest reaction order for H_2 and H_2O, pointing to a catalyst that has high conversion for hydrogen oxidation under dry conditions but becomes significantly inhibited by water. Regarding N_2O formation (reaction (III)), Pd/TiO_2 has the highest NO reaction order, while Pd/Al_2O_3 has the highest for H_2. This underlines the observed trend where Pd on metal oxide supports (Pd/Al_2O_3 and Pd/TiO_2) promotes N_2O formation more than Pd on zeolite supports [6,14]. Turning to NH_3 production (reaction (IV)), only Pd/TiO_2 was found to produce NH_3 which exhibited a low NO reaction order. This indicates that NH_3 formation in this case is unaffected by NO concentration and likely driven by other factors such as H_2 availability and water inhibition.

The model quality was evaluated using fitting quality indicators (adjusted R-squared, AIC, residual analysis (See Fig. 9)) and parameter robustness indicators (confidence intervals found in Fig. S13 of Supporting Information, and parameter pairwise correlation presented in Fig. 9). All proposed models yield adjusted R-squared values above 0.93, which is acceptable given the broad experimental range, the model simplification by using power-law kinetics, and the complexity of predicting multiple gas compounds at the outlet. The AIC values (Table 5) are similar compared to the two-reaction models, implying that the benefit of improved accuracy outweighs the cost of added complexity by adding more parameters [39].

Deviations in the normalized residual distribution, presented in Fig. 9 (left), remain under 10%, highlighting good predictive performance.

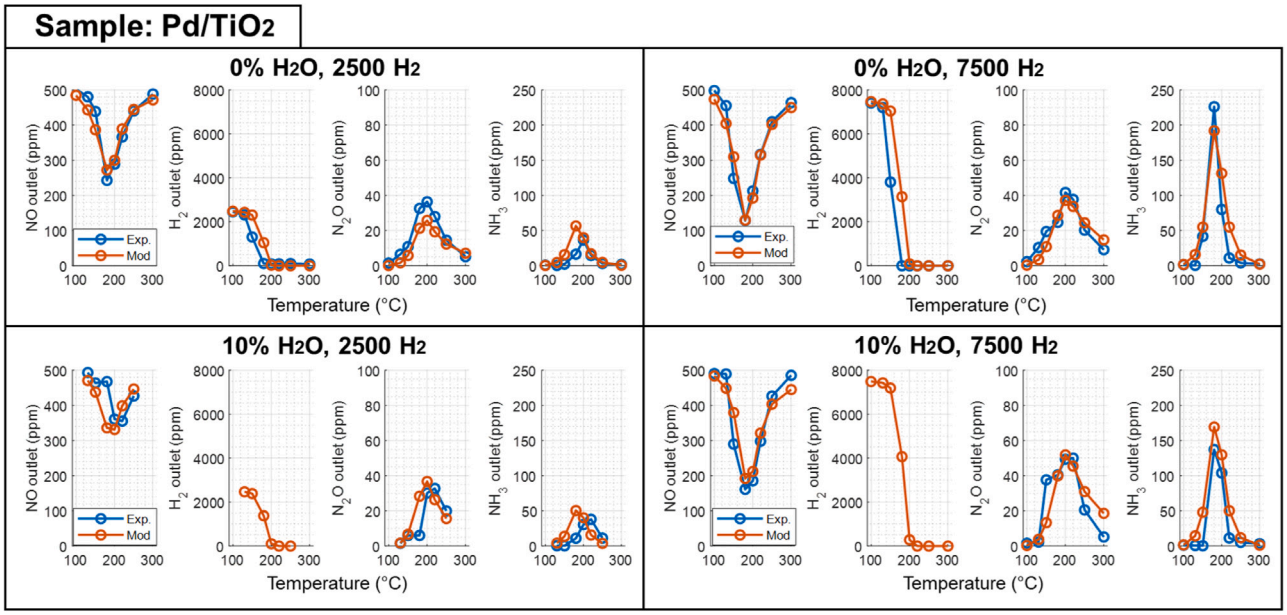

Fig. 7. Outlet gas composition for Pd/TiO_2 over different water concentrations: 0 and 10%, and different H_2/NO ratios: 5 and 15. NO feed concentration was 500 ppm for all the experiments. Blue line = experimental data. Red line = modeled data. Oxygen concentration was 10% and the space velocity (SV) was set at 65000 h^{-1}. It should be noted that the hydrogen concentration is estimated based on a hydrogen overall mass balance.

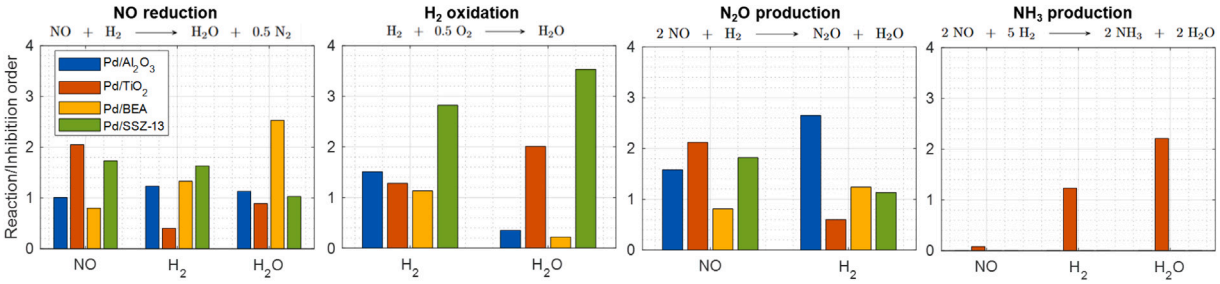

Fig. 8. Reaction order for NO, H_2, and Inhibition order for H_2O for reactions (I) (left) to (IV) (right) for the different catalyst samples. Reaction (IV) was observed only on Pd/TiO_2.

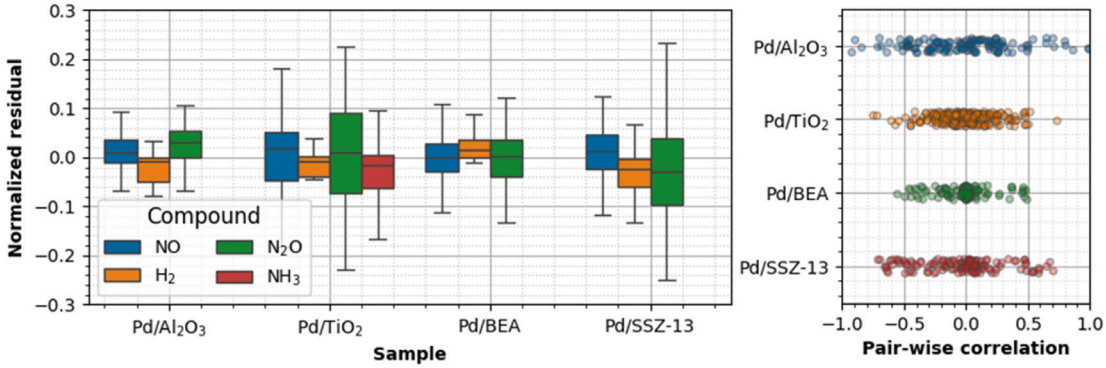

Fig. 9. (Left) Normalized residual distribution for the full reactor model for the studied H_2-SCR samples. The normalized residual was calculated for NO, H_2, N_2O and NH_3 comparing experimental and modeled values. The boxes represent the 25th–75th percentile range, with the median shown inside the box. Whiskers indicate the points beyond the 25th–75th percentile range, including outliers. (Right) Pair-wise correlation distribution for the models developed for all the H_2-SCR samples. Each point corresponds to individual pairwise values from the correlation matrix.

Larger deviations occur for N_2O predictions for Pd/TiO_2 and Pd/SSZ-13, and NO predictions for Pd/TiO_2 under low temperature, low H_2, and high water conditions. These deviations point to potential oversimplifications in the power-law kinetics, indicating that a more detailed model might be required in these specific experimental regions.

Pairwise correlations between model parameters were analyzed as an indicator of possible overfitting. For visualization, Fig. 9 (right) plots the non-diagonal elements of the pairwise correlation matrix projected onto one axis, where each point represents the correlation between two model parameters. The lowest correlations were found for Pd/BEA, while Pd/Al_2O_3 had some values close to 1. These correlations are

Table 5
Kinetic parameters for catalyst models for all the studied H_2-SCR samples. The last two rows are model quality indicators: R^2 and AIC.

	Pd/Al_2O_3	Pd/TiO_2	Pd/BEA	Pd/SSZ-13
A_1 (*)	2.13E+09	1.22E+10	1.02E+16	4.11E+13
Ea_1 (J/mol)	62100	56100	107000	79700
α_1	1.0	2.1	0.8	1.7
α_2	1.2	0.4	1.3	1.6
A_1^I (**)	3.9	1.1	0.8	0.5
Ea_1^I (J/mol)	5850	227	209	255
α_3	1.1	0.9	2.5	1.0
A_2 (*)	1.29E+16	2.41E+18	3.38E+17	2.25E+21
Ea_2 (J/mol)	128000	146000	121000	150000
β_1	1.5	1.3	1.1	2.8
A_2^I (**)	3.1	0.3	0.1	6.2
Ea_2^I (J/mol)	7070	1310	83100	14300
β_2	0.4	2.0	0.2	3.5
A_3 (*)	1.26E+18	2.46E+13	1.30E+16	1.36E+10
Ea_3 (J/mol)	127000	87000	119000	63400
δ_1	1.6	2.1	0.8	1.8
δ_2	2.7	0.6	1.2	1.1
A_4 (*)		3.11E+11		
Ea_4 (J/mol)		97300		
γ_1		0.1		
γ_2		1.2		
A_4^I (**)		138		
Ea_4^I (J/mol)		26200		
γ_3		2.2		
adj-R^2	0.93	0.96	0.98	0.93
AIC	-964	-974	-1190	-1040

REMARKS:
(*) Units of pre-exponential $[m^3]^{\sum z-1}[mol]^{1-\sum z}[s]^{-1}$ z=Rxn order
(**) Units of inhibition pre-exponential $[m^3]^{\sum z}[mol]^{-\sum z}$

expected to some degree, especially due to the interaction of parameters in the Arrhenius expression for the reaction rate constant. The higher correlations observed for Pd/Al_2O_3 reflects limited experimental information for the model, indicating that the optimal experimental region for model development is sample-dependent. Additional data could reduce parameter correlation and improve robustness.

Confidence intervals for all model parameters were calculated and presented in Fig. S13 in Supporting Information. Most parameters lie within the 95% confidence interval, with a few exceptions (especially for the NO reaction order in the N_2O formation reaction, and the water inhibition parameters in the H_2 oxidation on Pd/TiO_2 and Pd/BEA). Despite these limitations, the confidence intervals confirm the reliability of the model and the adequacy of the experimental design for extracting kinetic information.

4. Discussion

Support effects. Results from the catalyst characterization combined with the calibrated catalyst model allowed for evaluating the effect of the catalyst support and external mass transfer on NO conversion. All H_2-SCR catalyst samples were synthesized by the same method. However, this resulted in different dispersion and particle size distribution for Pd, which likely is a result of different surface area of the support and different interactions of the Pd precursors with the support. Higher NO conversion occurs due to the delayed H_2-to-H_2O reactions, which for Pd/TiO_2, could be a consequence of its low surface area, large Pd particle size, and low dispersion. However, the presence of metallic Pd, only present in Pd/TiO_2, enables a higher conversion to NO reactions and selectivity towards N_2 and NH_3.

The kinetic parameters derived from the H_2-SCR model for the different samples provide insight on how the support properties affect the reaction mechanism and Pd site nature. For the NO reduction (Reaction (I)), Pd/TiO_2 exhibits the highest reaction order for NO but the lowest for H_2. This indicates that the overall rate is governed by NO activation, since hydrogen species remain available on the surface due to H-spillover effects. In contrast, Pd/SSZ-13 shows high reaction orders for both NO and H_2, suggesting stronger adsorption that limits surface mobility and slows reaction turnover. Water inhibition is present across all samples, with Pd/BEA displaying the strongest effect, consistent with its adsorption strength and larger storage capacity, as observed in the NH_3-TPD experiments. Notably, Pd/Al_2O_3 presents a large pre-exponential factor, exceeding the other catalysts by several orders of magnitude. This large prefactor is associated with the formation of stabilized hydroxyl species on the support, which partially block NO and H_2 adsorption sites.

For H_2 oxidation (Reaction (II)), activation energies are comparable among all samples, indicating that the reaction is driven by Pd species that is present in all catalyst samples, which is the case for Pd in a high oxidation state [60,61]. Regarding reaction orders, Pd/BEA exhibits the lowest values, Pd/SSZ-13 the highest, while the metal oxides fall in between. This trend highlights the different behavior of the zeolite-based catalysts.

In the case for N_2O formation (Reaction (III)), high reaction orders were observed across all supports for one or both reactants, indicating that adsorption is the rate-limiting step and that the support governs the availability of adsorbed species. The difference in the reaction order for NO and H_2 further indicate support-dependent effects such as spillover and buffer of intermediates species (H, OH, NH_x). The distribution and stability of these intermediates vary with the support nature, directly influencing selectivity [6,14,55]. In addition, the support influences the Pd oxidation state, as seen by the XPS data (Table 3) which is also important for the catalyst performance.

NH_3 formation (Reaction (IV)) was only observed for Pd/TiO_2. The higher reaction order for hydrogen compared to NO indicates that NO is adsorbed and available on the surface, while hydrogen governs the overall rate through its dissociation, surface mobility, and subsequent formation of NH_x intermediates. Water inhibits NH_3 formation strongly, as evidenced by a high inhibition order. The proposed kinetic model includes inhibition terms for NO conversion to N_2 (Reaction I), H_2 oxidation (Reaction II), and NH_3 formation (Reaction IV), showing good agreement with experimental data in the 0%–10% water concentration range. Since the intended application involves higher water concentrations, the model identifies inhibition as the dominant effect of water. We have therefore performed simulations also for higher water contents, and the results are shown in Fig. S16 (Supporting Information), marked with extrapolation. Fig. S16 shows the conversions for all samples at different water concentrations (up to 20%) at 175 °C and an H_2/NO ratio of 10. Notably, the extent of inhibition varies among reactions and supports. It is also worth noting that N_2O formation was increased in the simulation, as it is not affected by water.

The support plays a relevant role in shaping the distribution, particle size, and oxidation state of Pd active sites, thereby controlling both the reaction mechanism and overall kinetics. In Pd/TiO_2, Pd exhibits low dispersion, large particles, and a lower oxidation state compared to the zeolite-supported samples, where Pd is more finely dispersed and at a higher oxidation state. These features suggest that metallic Pd provides higher intrinsic performance for NO conversion. Moreover, a support that allows an easy reduction of the active sites, such as Pd/TiO_2, can generate oxygen vacancies, promoting H_2O dissociation, and enhancing NO conversion [7–9]. The NH_3 formation, only present on Pd/TiO_2, suggests that metallic Pd promotes H_2 and H_2O dissociation, enabling hydrogen spillover in the support [62–64]. The adsorption characteristics affects the buffer capacity, the surface mobility and the selective interaction with other adsorbed species which is

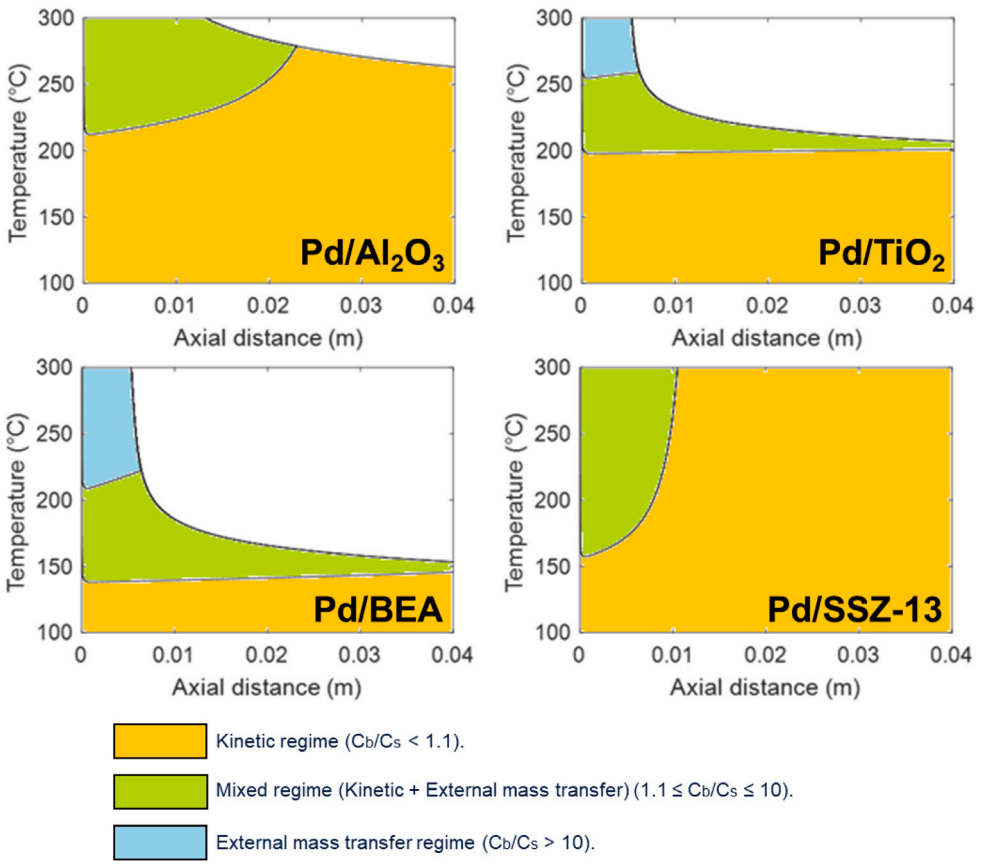

Fig. 10. Catalyst regimes based on H_2 concentration at different temperatures along the catalyst sample length for all H_2-SCR samples. Inlet gas composition NO=500 ppm, H_2=7500 ppm, H_2O=5%, O_2=10%. Yellow area = kinetic regime, green = mixed regime, blue = external mass transfer regime, blank = no reactions (H_2 fully consumed).

related to the low reaction orders. These trends emphasize adsorption properties as key factors governing NO conversion and selectivity.

Additionally, Pd/TiO_2 also exhibits a more diverse adsorption profile (Lewis and Brønsted), favoring dissociative over molecular adsorption, and stabilizing intermediates (H, OH, NH_x) through titania d-electron orbitals [65,66]. The role of adsorption strength extends to the formation and mobility of intermediates, central to H_2-SCR reaction pathways: stronger acid sites stabilize intermediates but reduce their mobility, thus limiting conversion, whereas weaker acidity promotes spillover and surface diffusion [67–70]. Particularly, TiO_2-supported catalysts have been shown to enhance H-spillover not only through weaker acidity but also via strong metal–support interactions with Pd, highlighting the interplay between adsorption strength, H-spillover, and support–metal interactions in determining catalytic performance [71,72].

External mass transfer. The full catalyst model (15) with the parameter values listed in Table 5 was used to explore the external mass transfer limitations of the different catalyst samples. Simulations at different temperature were run from which the hydrogen concentration in the bulk gas phase ($\bar{c}_{H_2}$) and in the washcoat (C_{H_2}) was extracted. Based on Joshi et al. [73], catalytic regime analysis can be done by two approaches, concentration-based and resistance-based, which yield comparable regime classification under identical conditions. In this study, the concentration-based approach was used, by comparing the ratio of the hydrogen bulk concentration ($\bar{c}_{H_2}$), and in the washcoat (C_{H_2}). A $\bar{c}_{H_2}/C_{H_2}$ ratio below 1.1 indicates a kinetic regime, values between 1.1 and 10 indicate a mixed regime, and ratios above 10 suggests control by external mass transfer [73].

Fig. 10 shows the kinetic regimes along the catalyst length at different temperatures for a feed ratio of $H_2/NO = 15$. The four panels refer to the four catalyst samples, with the colored areas indicating the different kinetic regimes. The white areas in Fig. 10 indicate full consumption of H_2 and, accordingly, a cease of the reactions.

At low temperatures, all samples are within the kinetic regime as indicated by the yellow colored areas. As temperature increases, the reaction rates increases and mass transfer becomes limiting as shown by the green and blue colored areas. This is especially the case at the front of the catalyst sample where, due to the high reactant concentrations, the reaction rate is large. As reactants are consumed along the catalyst length, the local rate decreases, causing a shift back to kinetic regime. This pattern is very pronounced for Pd/TiO_2 and Pd/BEA that exhibit external mass transfer limitations at high temperatures, primarily due to fast H_2 consumption. This fast H_2 consumption results in a cease of the reactions in the downstream section of the catalyst and, accordingly, in poor catalyst utilization. Pd/SSZ-13, being the least active catalyst, remains in the kinetic regime along most of the catalyst length. The high selectivity and low H_2 oxidation prevent a cease of the reaction. The Pd/Al_2O_3 is in the kinetic regime in most of the temperature region, with a mixed regime at high temperatures.

An in-depth analysis to quantify how external mass transfer affects NO conversion was done for Pd/TiO_2. Simulations were performed at 150, 250, and 300 °C, varying the external mass transfer coefficient. Results are shown in Fig. 11 where the panels in the upper row show the NO conversion along the catalyst length, with the different curves showing simulations where the mass transfer coefficient is increased/decreased by a certain factor with respect to k_m derived from the Sherwood correlation (4). At 150 °C (upper left panel) external mass transfer has little effect; the conversion begins to decline only when the mass transfer coefficient is reduced by a factor of ten. However, at 250 and 300 °C (middle and right upper panel) a

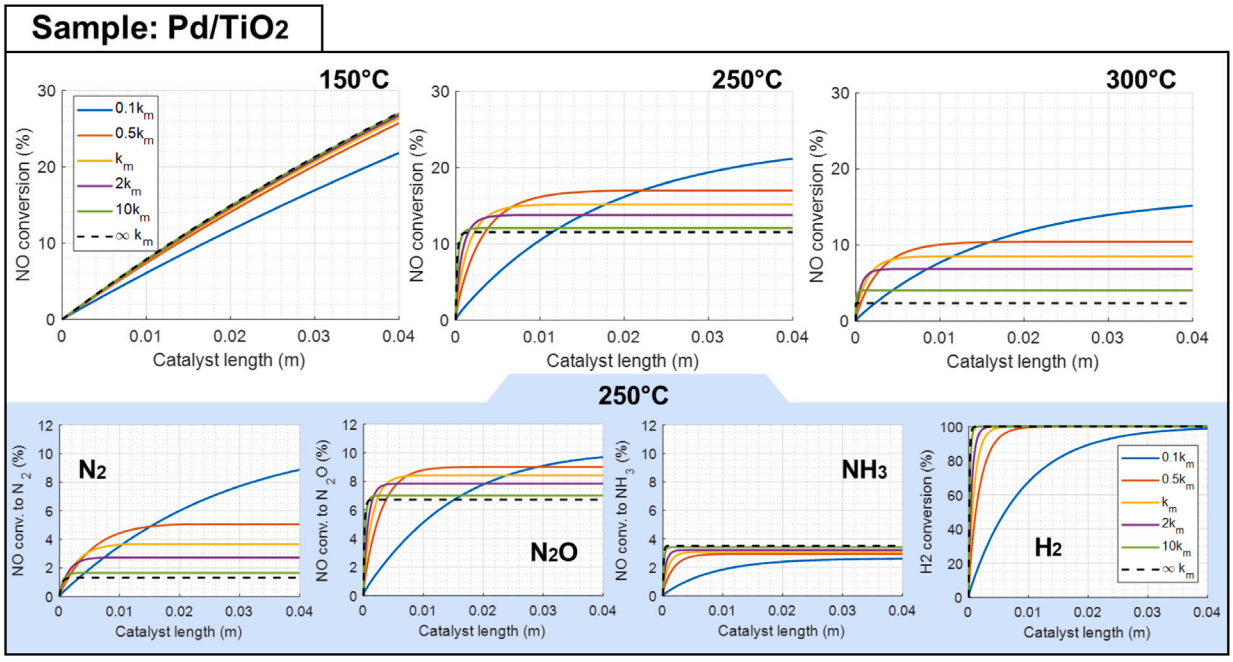

Fig. 11. Simulated NO conversion on Pd/TiO_2 at 150, 250 and 300 °C, and different external mass transfer coefficients, k_m. Inlet gas composition NO=500 ppm, H_2=7500 ppm, H_2O=5%, O_2=10%. Top row: Total NO conversion. Bottom row: Gas compound conversion at 250 °C.

pronounced increase in NO conversion upon a reduction in external mass transfer is observed, and the effect becomes more noticeable at higher temperatures.

This counterintuitive result is explained by reaction dynamics: external mass transfer introduces a resistance that slows down H_2 consumption, improving selectivity for NO reduction. As shown in the bottom row of Fig. 11, the delayed H_2 conversion leads to greater N_2 selectivity, minimal changes in N_2O, and reduced NH_3 formation. Essentially, slowing down the faster H_2 oxidation reaction provides more time for the slower NO reduction reactions to proceed, boosting the overall NO conversion. Gas compound conversions at 150 °C and 300 °C are shown in Fig. S17 (Supporting Information). The figure highlights a kinetic regime at low temperatures, with the strongest effect observed for H_2 oxidation. At high temperatures, NH_3 formation is the lowest.

These dynamic effects highlight how mass transfer affects the faster reactions, giving an advantage to the slower reactions. In H_2-SCR, external mass transfer suppresses H_2 oxidation, thus indirectly enhancing NO reduction. This effect on reaction rates can be achieved by manipulating the external mass transfer, reducing the gas velocity, increasing the diffusion path from bulk gas to catalyst surface, or modifying the catalyst surface properties. The simulations thus show that external mass transfer can enhance NO conversion and selectivity at high temperatures, but the magnitude and extent of this effect depend on the catalyst properties, especially on those affecting reaction kinetics.

5. Conclusions

This study compared the H_2-SCR catalytic performance of four Pd-supported catalysts over Al_2O_3, TiO_2, BEA zeolite, and SSZ-13 zeolite within the temperature range of 100–300 °C, under H_2/NO ratios of 5 to 15, in both dry and wet conditions. All catalysts showed their highest conversion at around 180 °C or 200 °C, confirming that Pd primarily operates within the medium-temperature range. In addition, Pd/TiO_2 exhibited the best performance among all the catalysts, maintaining good conversion even under wet conditions. Even though the samples were prepared by the same method, they exhibited different dispersion and particle size for Pd. CO chemisorption and TEM images showed that Pd/TiO_2 had the largest particle size and the lowest dispersion. Although this is generally unfavorable for catalytic performance, it primarily suppressed the competing hydrogen oxidation reaction. XPS analysis showed that only Pd/TiO_2 contained reduced Pd states, which explains its unique catalytic performance. Based on the experimental data, a power-law kinetic model was developed, assessing internal and external mass transfer effects for all four catalyst samples. The model considered NO reduction reactions producing N_2, N_2O, and NH_3, as well as the H_2 oxidation reaction. The model showed excellent agreement with the experimental data, with a narrow residual distribution for all the predicted compounds. The challenging experimental region for the model is under high water content, low H_2 concentration and low temperature which reflects the limitations of a power-law kinetic model where adsorbed species are not considered. The correlation between parameters and their confidence interval showed that there is no overfitting but the experimental region for maximizing information is sample dependent. The kinetic parameters from the model supports the experimental observations. It should be emphasized that external mass transfer played an important role in the reaction. At low temperatures, the reaction was primarily in the kinetic regime, but as the temperature increased, it gradually shifted towards mass transfer limitations. External mass transfer mainly restricted the fast H_2 oxidation reaction, especially for Pd/TiO_2. The delayed H_2 oxidation allowed more H_2 to remain available for NO reduction, thereby indirectly enhancing the overall performance of the H_2-SCR. In addition, NH_3 formation was observed exclusively on Pd/TiO_2 sample, and the corresponding reaction kinetics were also calculated. NH_3 can act as an additional reductant to assist in NO reduction, following the NH_3-SCR mechanism.

6. Nomenclature list

A	Pre-exponential factor, unit depends on reaction order
a_p	Washcoat surface area per volume of catalyst, m^2/m^3
C	Surface concentration, mol/m^3
$\overline{c}$	Bulk gas concentration, mol/m^3

D	Molecular diffusivity, $m^2/$ s
D_{eff}	Effective diffusivity, m^2/s
D_K	Knudsen diffusivity, m^2/s
Da	Damkohler number, –
d_a	Washcoat thickness, m
d_o	Open channel width, m
E_a	Activation energy, J/mol
k_m	Mass transfer coefficient, m/s
N	Number of sample points, –
N_{WP}	Weisz–Prater criterion, –
R	Gas constant, $R = 8.3145$ J/(mol.K)
r	Reaction rate, mol/(m^3.s)
r^{obs}	Apparent reaction rate, mol/(m^3.s)
S	Selectivity, –
Sh	Sherwood number, –
T	Temperature, K
v	Superficial gas flow velocity, m/s
X	Conversion, –
Y	Yield, –
y^{exp}	Experimental mole fraction, –
y^{mod}	Modeled mole fraction, –
z	Axial coordinate, m
z_{Sh}	Sherwood dimensionless axial coordinate, –
Subscripts	
i	Gas species
j	Reaction
Greek letters	
$\alpha, \beta, \delta, \gamma$	Reaction orders, –
ϵ	Washcoat porosity, –
ν	Stoichiometric coefficient, –
σ^2	Variance, –
τ	Washcoat tortuosity, –
ζ	Number of nitrogen atoms in molecule, –

CRediT authorship contribution statement

Andres F. Suarez-Corredor: Conceptualization, Catalyst performance test, Methodology, Modelling methodology, Software, Investigation, Writing – original draft, Visualization. **Jieling Shao:** Conceptualization, Catalyst preparation, Characterization methodology, Investigation, Writing – original draft. **Björn Westerberg:** Conceptualization, Writing – review & editing, Supervision. **Matthäus U. Bäbler:** Modelling methodology, Writing – original draft, Conceptualization, Supervision. **Louise Olsson:** Conceptualization, Writing – review & editing, Supervision.

Declaration of competing interest

The authors declare the following financial interests/personal relationships which may be considered as potential competing interests: Suarez-Corredor, Andres reports financial support, administrative support, equipment, chemicals, or supplies, and travel were provided by Scania CV AB. Westerberg, Bjorn reports financial support, administrative support, and travel were provided by Scania CV AB. If there are other authors, they declare that they have no known competing financial interests or personal relationships that could have appeared to influence the work reported in this paper.

Acknowledgments

This study has been funded by the Swedish Energy Agency, Sweden and carried out in collaboration with Volvo AB, Scania CV AB, and Johnson Matthey via a strategic vehicle research and innovation (FFI) project (P51458-1). We also acknowledge the assistance of Stefan Gustafsson, for assistance with the TEM measurements.

Appendix A. Supplementary data

Supplementary material related to this article can be found online at https://doi.org/10.1016/j.apcatb.2026.126855.

Data availability

Research Link Provided

Pd-based H2-SCR catalytic performance test on monoliths (Original data) (Mendeley Data)

References

[1] F. Dhainaut, S. Pietrzyk, P. Granger, Kinetics of the NO+ H_2 reaction over supported noble metal based catalysts: Support effect on their adsorption properties, Appl. Catal. B: Environ. 70 (1–4) (2007) 100–110.
[2] M. Borchers, K. Keller, P. Lott, O. Deutschmann, Selective catalytic reduction of NO_x with H_2 for cleaning exhausts of hydrogen engines: Impact of H_2O, O_2, and NO/H_2 ratio, Ind. Eng. Chem. Res. 60 (18) (2021) 6613–6626.
[3] M. Borchers, P. Lott, O. Deutschmann, Selective catalytic reduction with hydrogen for exhaust gas after-treatment of hydrogen combustion engines, Top. Catal. 66 (13) (2023) 973–984.
[4] J. Shao, P.H. Ho, D. Creaser, L. Olsson, Novel catalysts expanding the temperature range for NO selective catalytic reduction by H_2, Appl. Catal. O: Open 188 (2024) 206947.
[5] C. De Wolf, B. Nieuwenhuys, Oscillatory behaviour in the NO–hydrogen reactions over Pt-group metal surfaces, Catal. Today 70 (4) (2001) 287–300.
[6] L.-y. Huai, C.-z. He, H. Wang, H. Wen, W.-c. Yi, J.-y. Liu, NO dissociation and reduction by H_2 on Pd (111): A first-principles study, J. Catalysis 322 (2015) 73–83.
[7] K. Okumura, T. Motohiro, Y. Sakamoto, H. Shinjoh, Effect of combination of noble metals and metal oxide supports on catalytic reduction of NO by H_2, Surf. Sci. 603 (16) (2009) 2544–2550.
[8] Z. Liu, J. Li, S.I. Woo, Recent advances in the selective catalytic reduction of NO_x by hydrogen in the presence of oxygen, Energy & Environ. Sci. 5 (10) (2012) 8799–8814.
[9] G. Caravaggio, L. Nossova, R. Burich, Influence of supports on Pd catalysts for the selective catalytic reduction of NO_x with H_2 and CO, Emiss. Control. Sci. Technol. 2 (2016) 10–19.
[10] J. Shibata, M. Hashimoto, K.-i. Shimizu, H. Yoshida, T. Hattori, A. Satsuma, Factors controlling activity and selectivity for SCR of NO by hydrogen over supported platinum catalysts, J. Phys. Chem. B 108 (47) (2004) 18327–18335.
[11] M. Engelmann-Pirez, P. Granger, G. Leclercq, Investigation of the catalytic performances of supported noble metal based catalysts in the NO+ H_2 reaction under lean conditions, Catal. Today 107 (2005) 315–322.
[12] N. Macleod, R. Cropley, R.M. Lambert, Efficient reduction of NO_x by H_2 under oxygen-rich conditions over Pd/TiO_2 catalysts: an in situ DRIFTS study, Catal. Lett. 86 (2003) 69–75.
[13] A. Ueda, T. Nakao, M. Azuma, T. Kobayashi, Two conversion maxima at 373 and 573k in the reduction of nitrogen monoxide with hydrogen over Pd/TiO_2 catalyst, Catal. Today 45 (1–4) (1998) 135–138.
[14] T. Nanba, C. Kohno, S. Masukawa, J. Uchisawa, N. Nakayama, A. Obuchi, Improvements in the N_2 selectivity of Pt catalysts in the NO–H_2–O_2 reaction at low temperatures, Appl. Catal. B: Environ. 46 (2) (2003) 353–364.
[15] N. Macleod, R. Cropley, J.M. Keel, R.M. Lambert, Exploiting the synergy of titania and alumina in lean NO_x reduction: in situ ammonia generation during the $Pd/TiO_2/Al_2O_3$–catalysed $H_2/CO/NO/O_2$ reaction, J. Catalysis 221 (1) (2004) 20–31.
[16] J.-B. Yang, O.-Z. Fu, D.-Y. Wu, S.-D. Wang, DRIFTS study of NO–H_2 reaction over Pd/Al_2O_3 with excess oxygen, Appl. Catal. B: Environ. 49 (1) (2004) 61–65.
[17] F. Dhainaut, S. Pietrzyk, P. Granger, NO + H_2 reaction on Pd/Al_2O_3 under lean conditions: Kinetic study, Top. Catal. 42 (2007) 135–141.
[18] T.J. Eldridge, M. Borchers, P. Lott, J.-D. Grunwaldt, D.E. Doronkin, Elucidating the role of the state of Pd in the H_2-SCR of NO_x by operando XANES and DRIFTS, Catal. Sci. Technol. 14 (15) (2024) 4198–4210.
[19] E.K. Dann, E.K. Gibson, R.H. Blackmore, C.R.A. Catlow, P. Collier, A. Chutia, T.E. Erden, C. Hardacre, A. Kroner, M. Nachtegaal, et al., Structural selectivity of supported Pd nanoparticles for catalytic NH_3 oxidation resolved using combined operando spectroscopy, Nat. Catal. 2 (2) (2019) 157–163.
[20] Z. Savva, K.C. Petallidou, C.M. Damaskinos, G.G. Olympiou, V.N. Stathopoulos, A.M. Efstathiou, H_2-SCR of NO_x on low-SSA CeO_2-supported Pd: The effect of Pd particle size, Appl. Catal. A: Gen. 615 (2021) 118062.
[21] P. Cheng, M. Shen, W. Li, G. Shen, NO/H_2 reaction pathway and kinetic model on Pd/Al_2O_3 in passive SCR for hydrogen ICE aftertreatment, Int. J. Hydrog. Energy 142 (2025) 366–375.

[22] A. Lindholm, N.W. Currier, A. Yezerets, L. Olsson, A kinetic study of NO_x reduction over Pt/SiO_2 model catalysts with hydrogen as the reducing agent, Top. Catal. 42 (2007) 83–89.

[23] A. Lindholm, N.W. Currier, J. Li, A. Yezerets, L. Olsson, Detailed kinetic modeling of NO_x storage and reduction with hydrogen as the reducing agent and in the presence of CO_2 and H_2O over a Pt/Ba/Al catalyst, J. Catalysis 258 (1) (2008) 273–288.

[24] Z. Yao, L. Li, X. Liu, K.N. Hui, L. Shi, F. Zhou, M. Hu, K. Hui, Mechanistic insights into NO-H_2 reaction over Pt/boron-doped graphene catalyst, J. Hazard. Mater. 406 (2021) 124327.

[25] C. Hahn, M. Endisch, F.J. Schott, S. Kureti, Kinetic modelling of the NO_x reduction by H_2 on $Pt/WO_3/ZrO_2$ catalyst in excess of O_2, Appl. Catal. B: Environ. 168 (2015) 429–440.

[26] S.Y. Joshi, Y. Ren, M.P. Harold, V. Balakotaiah, Determination of kinetics and controlling regimes for H_2 oxidation on Pt/Al2O3 monolithic catalyst using high space velocity experiments, Appl. Catal. B: Environ. 102 (3–4) (2011) 484–495.

[27] B. Frank, G. Emig, A. Renken, Kinetics and mechanism of the reduction of nitric oxides by H_2 under lean-burn conditions on a Pt–Mo–Co/α-Al_2O_3 catalyst, Appl. Catal. B: Environ. 19 (1) (1998) 45–57.

[28] J. Shao, P.H. Ho, W. Di, D. Creaser, L. Olsson, Pt-based catalysts for NO_x reduction from H_2 combustion engines, Catal. Sci. Technol. 14 (11) (2024) 3219–3234.

[29] A.F. Suarez-Corredor, M.U. Babler, L. Olsson, M. Skoglundh, B. Westerberg, Characterization method for gas flow reactor experiments—NH_3 adsorption on vanadium-based scr catalysts, Ind. Eng. Chem. Res. 60 (30) (2021) 11399–11411.

[30] E. Tronconi, P. Forzatti, Adequacy of lumped parameter models for SCR reactors with monolith structure, AIChE J. 38 (2) (1992) 201–210.

[31] B.E. Poling, J.M. Prausnitz, O. John Paul, R.C. Reid, The Properties of Gases and Liquids, vol. 5, McGraw-Hill New York, 2001.

[32] R. Hayes, S. Kolaczkowskib, P. Li, S. Awdry, Evaluating the effective diffusivity of methane in the washcoat of a honeycomb monolith, Appl. Catal. B: Environ. 25 (2–3) (2000) 93–104.

[33] B. Mitra, D. Kunzru, Washcoating of different zeolites on cordierite monoliths, J. Am. Ceram. Soc. 91 (1) (2008) 64–70.

[34] S. Kato, S. Yamaguchi, T. Uyama, H. Yamada, T. Tagawa, Y. Nagai, T. Tanabe, Characterization of secondary pores in washcoat layers and their effect on effective gas transport properties, Chem. Eng. J. 324 (2017) 370–379.

[35] J.M. Thomas, W.J. Thomas, Principles and practice of Heterogeneous Catalysis, John Wiley & Sons, 2014.

[36] N.R. Draper, H. Smith, Applied Regression Analysis, vol. 326, John Wiley & Sons, 1998.

[37] A.-N. Spiess, N. Neumeyer, An evaluation of R2 as an inadequate measure for nonlinear models in pharmacological and biochemical research: a Monte Carlo approach, BMC Pharmacol. 10 (1) (2010) 6.

[38] T.O. Kva Lseth, Note on the R2 measure of goodness of fit for nonlinear models, Bull. Psychon. Soc. 21 (1) (1983) 79–80.

[39] J. Cavanaugh, A. Neath, The Akaike information criterion: Background, derivation, properties, application, interpretation, and refinements, WIREs Computational Statistics 11 (3) (2019) e1460.

[40] C. Coney, C. Stere, P. Millington, A. Raj, S. Wilkinson, M. Caracotsios, G. McCullough, C. Hardacre, K. Morgan, D. Thompsett, et al., Spatially-resolved investigation of the water inhibition of methane oxidation over palladium, Catal. Sci. Technol. 10 (6) (2020) 1858–1874.

[41] G. Bergeret, P. Gallezot, Particle size and dispersion measurements, in: Handbook of Heretogeneous Catalysis, vol. 2, Wiley-VCH, 2008, pp. 738–765.

[42] Q. Sun, N. Wang, J. Yu, Advances in catalytic applications of zeolite-supported metal catalysts, Adv. Mater. 33 (51) (2021) 2104442.

[43] S. Tauster, S. Fung, R.L. Garten, Strong metal-support interactions. Group 8 noble metals supported on titanium dioxide, J. Am. Chem. Soc. 100 (1) (1978) 170–175.

[44] P. Weerachawanasak, O. Mekasuwandumrong, M. Arai, S.-I. Fujita, P. Praserthdam, J. Panpranot, Effect of strong metal-support interaction on the catalytic performance of Pd/TiO_2 in the liquid-phase semihydrogenation of phenylacetylene, J. Catalysis 262 (2) (2009) 199–205.

[45] J. Herrmann, M. Gravelle-Rumeau-Maillot, P. Gravelle, A microcalorimetric study of metal-support interaction in the Pt/TiO_2 system, J. Catalysis 104 (1) (1987) 136–146.

[46] J. Santos, J. Phillips, J. Dumesic, Metal-support interactions between iron and titania for catalysts prepared by thermal decomposition of iron pentacarbonyl and by impregnation, J. Catalysis 81 (1) (1983) 147–167.

[47] S. Gates-Rector, T. Blanton, The powder diffraction file: a quality materials characterization database, Powder Diffr. 34 (4) (2019) 352–360.

[48] O. Mihai, L. Trandafilović, T. Wentworth, F.F. Torres, L. Olsson, The effect of Si/Al ratio for Pd/BEA and Pd/SSZ-13 used as passive NO_x adsorbers, Top. Catal. 61 (2018) 2007–2020.

[49] Z. Chen, E. Vorobyeva, S. Mitchell, E. Fako, M.A. Ortuño, N. López, S.M. Collins, P.A. Midgley, S. Richard, G. Vilé, et al., A heterogeneous single-atom palladium catalyst surpassing homogeneous systems for Suzuki coupling, Nature Nanotechnology 13 (8) (2018) 702–707.

[50] D. Chen, H. Lei, W. Xiong, Y. Li, X. Ji, J.-Y. Yang, B. Peng, M. Fu, P. Chen, D. Ye, Unravelling phosphorus-induced deactivation of Pd-SSZ-13 for passive NO_x adsorption and CO oxidation, ACS Catal. 11 (22) (2021) 13891–13901.

[51] J.F. Moulder, W.F. Stickle, P.E. Sobol, K.D. Bomben, Handbook of X-ray photoelectron spectroscopy: a reference book of standard spectra for identification and interpretation of XPS data, 1992, 2000, pp. 232–233.

[52] M.-S. Kim, S.-H. Chung, C.-J. Yoo, M.S. Lee, I.-H. Cho, D.-W. Lee, K.-Y. Lee, Catalytic reduction of nitrate in water over $Pd\text{-}Cu/TiO_2$ catalyst: effect of the strong metal-support interaction (SMSI) on the catalytic activity, Appl. Catal. B: Environ. 142 (2013) 354–361.

[53] J. Bronsted, Acid and Basic catalysis, Chem. Rev. 5 (3) (1928) 231–338.

[54] Z. Hu, R.T. Yang, 110th anniversary: Recent progress and future challenges in selective catalytic reduction of NO by H_2 in the presence of O_2, Ind. Eng. Chem. Res. 58 (24) (2019) 10140–10153.

[55] X. Li, X. Zhang, Y. Xu, Y. Liu, X. Wang, Influence of support properties on H_2 selective catalytic reduction activities and N_2 selectivities of Pt catalysts, Chin. J. Catal. 36 (2) (2015) 197–203.

[56] B.M. Weiss, E. Iglesia, Mechanism and site requirements for NO oxidation on Pd catalysts, J. Catalysis 272 (1) (2010) 74–81.

[57] X. Auvray, L. Olsson, Stability and activity of Pd-, Pt- and Pd-Pt catalysts supported on alumina for NO oxidation, Appl. Catal. B: Environ. 168 (2015) 342–352.

[58] H.S. Fogler, Elements of Chemical Reaction Engineering, Pearson Educacion, 1999.

[59] I. Chorkendorff, J.W. Niemantsverdriet, Concepts of Modern Catalysis and Kinetics, John Wiley & Sons, 2017.

[60] N. Martin, M. Van den Bossche, H. Gronbeck, C. Hakanoglu, J. Gustafson, S. Blomberg, M.A. Arman, A. Antony, R. Rai, A. Asthagiri, et al., Dissociative adsorption of hydrogen on PdO (101) studied by HRCLS and DFT, J. Phys. Chem. C 117 (26) (2013) 13510–13519.

[61] S.C. Su, J.N. Carstens, A.T. Bell, A study of the dynamics of Pd oxidation and PdO reduction by H_2 and CH_4, J. Catalysis 176 (1) (1998) 125–135.

[62] G.-C. Wang, S.-X. Tao, X.-H. Bu, A systematic theoretical study of water dissociation on clean and oxygen-preadsorbed transition metals, J. Catalysis 244 (1) (2006) 10–16.

[63] R. Prins, Hydrogen spillover. Facts and fiction, Chem. Rev. 112 (5) (2012) 2714–2738.

[64] W.C. Conner Jr., J.L. Falconer, Spillover in heterogeneous catalysis, Chem. Rev. 95 (3) (1995) 759–788.

[65] S. Bagheri, N. Muhd Julkapli, S. Bee Abd Hamid, Titanium dioxide as a catalyst support in heterogeneous catalysis, Sci. World J. 2014 (1) (2014) 727496.

[66] I.E. Wachs, B.M. Weckhuysen, Structure and reactivity of surface vanadium oxide species on oxide supports, Appl. Catal. A: Gen. 157 (1–2) (1997) 67–90.

[67] Q. Yu, M. Richter, F. Kong, L. Li, G. Wu, N. Guan, Selective catalytic reduction of NO by hydrogen over Pt/ZSM-35, Catal. Today 158 (3–4) (2010) 452–458.

[68] G.G. Olympiou, A.M. Efstathiou, Industrial NO_x control via H_2-SCR on a novel supported-Pt nanocatalyst, Chem. Eng. J. 170 (2–3) (2011) 424–432.

[69] M. Niwa, N. Katada, New method for the temperature-programmed desorption (TPD) of ammonia experiment for characterization of zeolite acidity: A review, Chem. Rec. 13 (5) (2013) 432–455.

[70] M. Benkhaled, C. Descorme, D. Duprez, S. Morin, C. Thomazeau, D. Uzio, Study of hydrogen surface mobility and hydrogenation reactions over alumina-supported palladium catalysts, Appl. Catal. A: Gen. 346 (1–2) (2008) 36–43.

[71] Z. Liu, B. Jia, Y. Zhang, M. Haneda, Engineering the metal–support interaction on Pt/TiO_2 catalyst to boost the H_2-SCR of NO_x, Ind. Eng. Chem. Res. 59 (31) (2020) 13916–13922.

[72] S. Xu, Y. Zhang, C. Hardacre, Z. Liu, Enhanced catalytic activity of Pd supported on TiO_2 nanowire for the H_2-SCR of NO_x in the presence of oxygen, ACS Sustain. Chem. Eng. 11 (28) (2023) 10453–10461.

[73] S.Y. Joshi, M.P. Harold, V. Balakotaiah, Overall mass transfer coefficients and controlling regimes in catalytic monoliths, Chem. Eng. Sci. 65 (5) (2010) 1729–1747.